MASTERARBEIT / MASTER’S THESIS

Titel der Masterarbeit / Title of the Master‘s Thesis

„Spatial Analysis of Intra-Annual Reed Ecosystem Dynamics at Lake Neusiedl using RGB Drone Imagery and Deep Learning“

verfasst von / submitted by

Claudia Buchsteiner BSc

angestrebter akademischer Grad / in partial fulfilment of the requirements for the degree of

Master of Science (MSc)

Wien, 2024 / Vienna 2024

Studienkennzahl lt. Studienblatt / Degree programme code as it appears on the student record sheet:	UA 066 856
Studienrichtung lt. Studienblatt / Degree programme as it appears on the student record sheet:	Masterstudium Kartographie und Geoinformation
Betreut von / Supervisor:	Ass.-Prof. Mag. Dr. Andreas Riedl

Publication confirmation / Bestätigung der Publikation


remote sensing

an Open Access Journal by MDPI

Indexed in: Ei Compendex

CITESCORE 7.9

IMPACT FACTOR 5.0

CERTIFICATE OF PUBLICATION

Certificate of publication for the article titled:

Spatial Analysis of Intra-Annual Reed Ecosystem Dynamics at Lake Neusiedl Using RGB Drone Imagery and Deep Learning

Authored by:

Claudia Buchsteiner; Pamela Alessandra Baur; Stephan Glatzel

Published in:

Remote Sens. **2023**, Volume 15, Issue 16, 3961

MDPI Academic Open Access Publishing since 1996

Basel, October 2023

Citation recommendation (MDPI and ACS Style)

Buchsteiner, C.; Baur, P.A.; Glatzel, S. Spatial Analysis of Intra-Annual Reed Ecosystem Dynamics at Lake Neusiedl Using RGB Drone Imagery and Deep Learning. *Remote Sens.* **2023**, *15*, 3961. https://doi.org/10.3390/rs15163961

Data Availability Statement

Data are available from the PHAIDRA Repository https://doi.org/10.25365/phaidra.397.

Table of contents

List of figures

List of tables

List of appendices

List of abbreviations

AI	Artificial Intelligence
APOS	Austrian Positioning Service
CNN	Convolutional Neural Network
DL	Deep Learning
DOY	Day of the Year
EC	Eddy Covariance
FN	False Negative
FP	False Positive
GCC	Green Chromatic Coordinates
GCP	Ground Control Points
GNSS	Global Navigation Satellite System
GPU	Graphics Processing Unit
GSD	Ground Sampling Distance
IoU	Intersection over Union
LCC	Land Cover Classification
LTER	Long-Term Ecological Research
ML	Machine Learning
OA	Overall Accuracy
OBIA	Object-Based Image Analysis
RGB	Red-Green-Blue
RMSE	Root Mean Square Error
ROI	Region of Interest
RTK	Real-Time Kinematics
SD	Standard Deviation
SfM	Structure from Motion
TP	True Positive
UAS	Unmanned Aerial System
UAV	Unmanned Aerial Vehicle

Acknowledgements

I would like to express my thanks to my supervisor Andreas Riedl who gave me a lot of creative freedom during the development of this thesis. My thanks go to Stephan Glatzel and the Geoecology group, whose research activities provided the framework for my thesis and motivated me to make a meaningful contribution to ongoing research. A profound thank you goes to Pamela Baur, who has been my mentor, guide and motivator from the very beginning to the very end of my thesis. It has been a great pleasure to work with you and it was you who made me aim higher and bring out the best in me - thank you so much!

I am deeply grateful to the taxpayers of our country because student grants have made my educational journey possible and enabled me to pursue my academic ambitions. Thank you for investing in the future of our country.

I want to say a big thank you to my dear friends for their constant support and belief in me, even and especially in times when I doubted myself. I am truly blessed to have such incredible people in my life.

I would like to thank my wife Margot from the bottom of my heart for her tireless support in countless ways. Your love, understanding and believe in me were my anchor through my university years and especially through this master’s thesis. I am infinitely grateful to have you by my side, that you are my home, my refuge, the place where I get my cuddles and the most delicious food.

Abstract

The reed belt of Lake Neusiedl, covering half the size of the lake, is subject to massive changes due to the strong decline of the water level over the last several years, especially in 2021. In this study, we investigated the spatial and temporal variations within a long-term ecosystem research (LTER) site in a reed ecosystem at Lake Neusiedl in Austria under intense drought conditions. Spatio-temporal data sets from May to November 2021 were produced to analyze and detect changes in the wetland ecosystem over a single vegetation period. High-resolution orthomosaics processed from RGB imagery taken with an unmanned aerial vehicle (UAV) served as the basis for land cover classification and phenological analysis. An image annotation workflow was developed, and deep learning techniques using semantic image segmentation were applied to map land cover changes. The trained models delivered highly favorable results in terms of the assessed performance metrics. When considering the region between their minima and maxima, the water surface area decreased by 26.9%, the sediment area increased by 23.1%, and the vegetation area increased successively by 10.1% over the investigation period. Phenocam data for lateral phenological monitoring of the vegetation development of Phragmites australis was directly compared with phenological analysis from aerial imagery. This study reveals the enormous dynamics of the reed ecosystem of Lake Neusiedl, and additionally confirms the importance of remote sensing via drone and the strengths of deep learning for wetland classification.

Kurzfassung

Der Schilfgürtel des Neusiedler Sees, der die Hälfte der Fläche des Sees bedeckt, ist aufgrund des starken Rückgangs des Wasserspiegels in den letzten Jahren, insbesondere im Jahr 2021, massiven Veränderungen unterworfen. In dieser Studie untersuchten wir die räumlichen und zeitlichen Variationen innerhalb einer Langzeit-Ökosystem-Forschungsstation (LTER) in einem Schilf-Ökosystem am Neusiedler See in Österreich unter intensiven Trockenheitsbedingungen. Es wurden räumlich-zeitliche Datensätze von Mai bis November 2021 erstellt, um Veränderungen im Feuchtgebietsökosystem über eine Vegetationsperiode hinweg zu analysieren. Hochauflösende Orthomosaike aus RGB-Bildern, die mit einem unbemannten Luftfahrzeug (UAV) aufgenommen wurden, dienten als Grundlage für die Klassifizierung der Bodenbedeckung und die phänologische Analyse. Um Veränderungen der Bodenbedeckung kartieren zu können wurde ein Arbeitsablauf für die Bild-Annotation entwickelt und Deep-Learning Methoden mit semantischer Bildsegmentierung angewandt. Die trainierten Modelle lieferten im Hinblick auf die Leistungsmetriken äußerst günstige Ergebnisse. Betrachtet man die Region zwischen ihren Minima und Maxima, so verringerte sich die Wasseroberfläche um 26.9 %, die Sedimentfläche nahm um 23.1 % zu und die Vegetationsfläche dehnte im Untersuchungszeitraum sukzessive um 10.1 % aus. Phenocam-Daten zur lateralen phänologischen Beobachtung der Vegetationsentwicklung von *Phragmites australis* (Schilf) wurden direkt mit phänologischen Analysen aus den Luftbildern verglichen. Diese Studie zeigt die enorme Dynamik des Schilfökosystems des Neusiedler Sees auf und bestätigt darüber hinaus die Bedeutung der Fernerkundung mittels Drohne und die Stärken von Deep Learning für die Feuchtgebietsklassifizierung.

Graphical Abstract / Grafische Kurzfassung

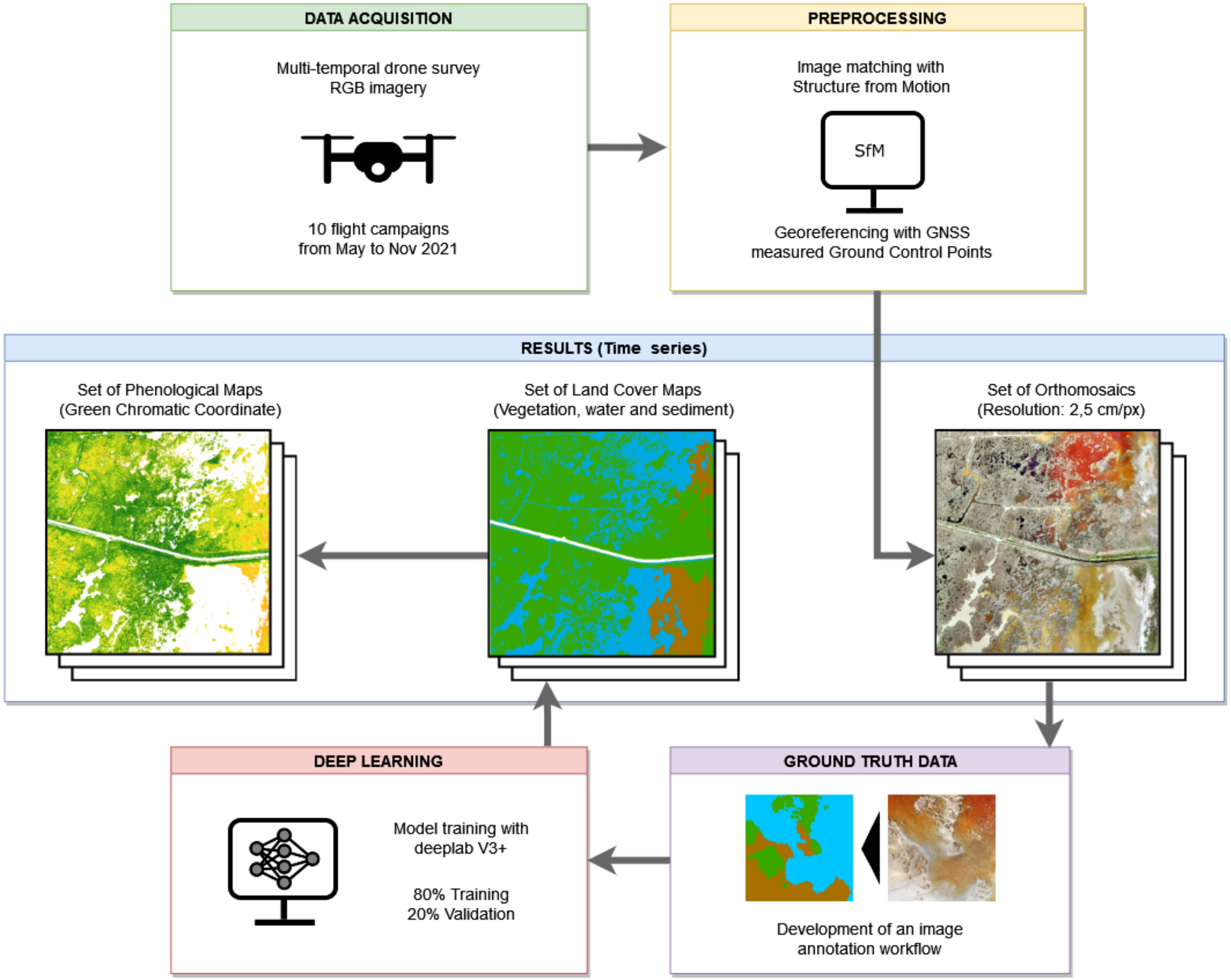

1 Introduction

Wetlands are of immense importance as highly valuable ecosystems intertwined with human welfare. They fulfill an indispensable function in preserving biodiversity, purifying water, enhancing resilience against storm surges, sequestering carbon, regulating microclimates, and more (Mitsch et al. 2015). Reed belts in particular have ecological importance as habitats for highly specialized species and as a buffer zone for lakes and rivers. They provide an indispensable habitat for waterfowl (Čížková et al. 2023) and invertebrates. Reed shoots are a food source for herbivores, and in an aquatic setting reed stands provide a spawning ground and nursery for fish (Kallasvuo et al. 2011), prevent erosion, and stabilize the strength of the bank (Yu et al. 2020). The reed belt of Lake Neusiedl is the second largest coherent reed ecosystem in Europe after the Danube Delta, and for nature conservation reasons it is a very important habitat for many protected bird species (Nemeth et al. 2022). Lake Neusiedl is a long-term ecological research (LTER) site contributing to a pan-European research network seeking to better understand the structures and functions of ecosystems (https://lter-austria.at, accessed on 5 August 2023) (Mirtl et al. 2015). Remote sensing imagery is required to spatially visualize and analyze such sites and understand the effects of global changes at the local scale (Díaz-Delgado et al. 2019).

The following aerial image analysis studies of 1979, 2008, 2018/2019 addressed the extent of the reed belt of Lake Neusiedl. The Austrian reed belt of Lake Neusiedl was mapped as early as 1979 to study the vegetation damage and age classes of reeds through color infrared aerial photography (Csaplovics 1982). The study of August 1979 was carried out on the basis of a three-feature classification utilizing the density, height, and vitality classes. In contrast, the reed mapping of August 2008 used a continuous stereoscopic (visual) interpretation of assigned pairs of aerial photographs (stereo pairs) (Csaplovics et al. 2011). Although the total reed belt area of Lake Neusiedl increased between 1979 and 2008, the reed stocks within the reed belt area decreased (Csaplovics et al. 2011). The authors showed that in the year 2008 around 12.5% of the total reed belt was covered by humic water. For the same aerial photographs from August 2008, the study of (Nemeth et al. 2014) measured 19% water coverage in the reed belt; the authors included small water areas with a spatial resolution of 0.25 m² as water. In (Csaplovics et al. 2014), NDVI-inclusive airborne optical imaging was used in support of habitat ecological monitoring of the Austrian reed belt in a study investigating the different reed classes and habitat-specific dependencies of different bird species. The reed belt coverage is clearly higher in the Hungarian part of Lake Neusiedl (83.6% in 2007, which included grassland with reed coverage of around 5%) as compared to the Austrian part (around 50%). The Hungarian reed belt area decreased slightly, by

0.8% from 1979 to 2007, due to the increase in “feltöltés” (embankment/levee areas), though not in open-water areas (Markus et al. 2012). In 2007, only 1.2% of the Hungarian part of Lake Neusiedl was covered by humic water (Markus et al. 2012), which is a very small share compared to the Austrian reed belt; see (Nemeth et al. 2014). Márkus et al. recognized a strong degradation of the Hungarian reed belt due to damage caused by the harvesting machines, which were called die-back sites in (Dinka et al. 2010); these were observed in the Austrian part, though to a lesser extent, in (Csaplovics et al. 2011). One study from 2018/2019 used Sentinel-2b data to monitor the age of reed stands, finding that the dominant age class (especially in the eastern reed belt) was areas older than 14 years (Nemeth et al. 2022).

Previous studies analysing the spatial patterns of the reed belt have been based on either low-resolution satellite data or medium-resolution aerial imagery derived from costly single-flight surveys. To date, the spatial patterns of the reed belt have not been studied with high-resolution data. In addition, little is known about the temporal dynamics of the surface structure of the reed belt within a one-year time frame. To address this gap, in this study we used an unmanned aerial vehicle (UAV) to generate a time series of high-resolution aerial imagery data. A series of ten UAV-derived orthomosaics provided the basis for land cover classification and phenological analysis to track changes in intra-annual variability in the spatial dynamics of the reed ecosystem over the growing season of 2021, which is of particular interest due to the intense drought during the study period. The region of Lake Neusiedl has been facing drought conditions since the summer of 2015, causing the average water level of the lake to decrease, especially in recent years (Hackl et al. 2023).

The main objectives of this work are:

- To provide a detailed workflow for land cover classification of high-resolution orthoimagery using deep learning image segmentation.
- To reveal the spatial and temporal variability of a reed ecosystem under intensive drought conditions.
- To disclose the phenological stages of *Phragmites australis* in the reed stands of Lake Neusiedl over the 2021 vegetation period.

2 Theoretical Framework

This chapter is intended to provide an overview of the theoretical and methodological background of the present study. It provides an insight into the fundamentals of remote sensing and gives a deep dive into the photogrammetric technique applied in this work. In addition, techniques for classifying land cover in the context of artificial intelligence will be discussed.

2.1 Remote Sensing

The term remote sensing summarizes the scientific techniques for collecting information and data about the earth's surface without the need for direct physical contact. The utilization of various sensors mounted on airborne or satellite-based platforms enable the systematic acquisition of electromagnetic radiation emitted or reflected by the earth's surface. Spatial and spectral information can be extracted and analysed in different ways to help understand environmental phenomena, such as land cover dynamics, vegetation vitality, terrain characteristics and many more. The integration of remote sensing data in geographic information systems (GIS) provides the basis for various scientific disciplines, especially geography, environmental science, agriculture and meteorology. Over the last decades remote sensing has contributed to a deeper understanding of the complex and dynamic systems of the earth. The integration of continuously developing technologies and analytical methods in remote sensing has increased its importance in monitoring, managing and understanding the interactions within the earth’s ecosystems and thus contributed significantly to both scientific research and decision-making. (Campbell 2002, Chuvieco et al. 2020)

2.1.1 Sensor Characteristics

A categorisation of remote sensor systems can be made according to the source of the received radiation: active and passive. Passive systems use only the electromagnetic radiation found in nature. This can be solar radiation that is reflected by the earth's surface or the radiation emitted by a body due to its surface temperature. Active systems, on the other hand, emit radiation themselves like (LiDAR and radar systems) and receive the portion reflected by the terrain with their sensor (see Figure 1). A further distinction can be made between remote sensing systems based on the spectrum of wavelengths they can receive when collecting data. The terms channel or band describe a range of different wavelengths which can be captured and recorded by a sensor. If a sensor records values in a few discrete bands, this is referred to as a multispectral sensor. Common earth observation satellite systems like Landsat or Sentinel are typical multispectral sensors with a maximum of 11 and 13 bands respectively. Instruments that are able to create images with a high level of spectral detail are called hyperspectral sensors. One of the earliest hyperspectral sensors is the AVIRIS (Airborne Visible/Infrared Imaging Spectrometer), which is able to deliver 224 contiguous spectral bands, for example. (Albertz 2007)

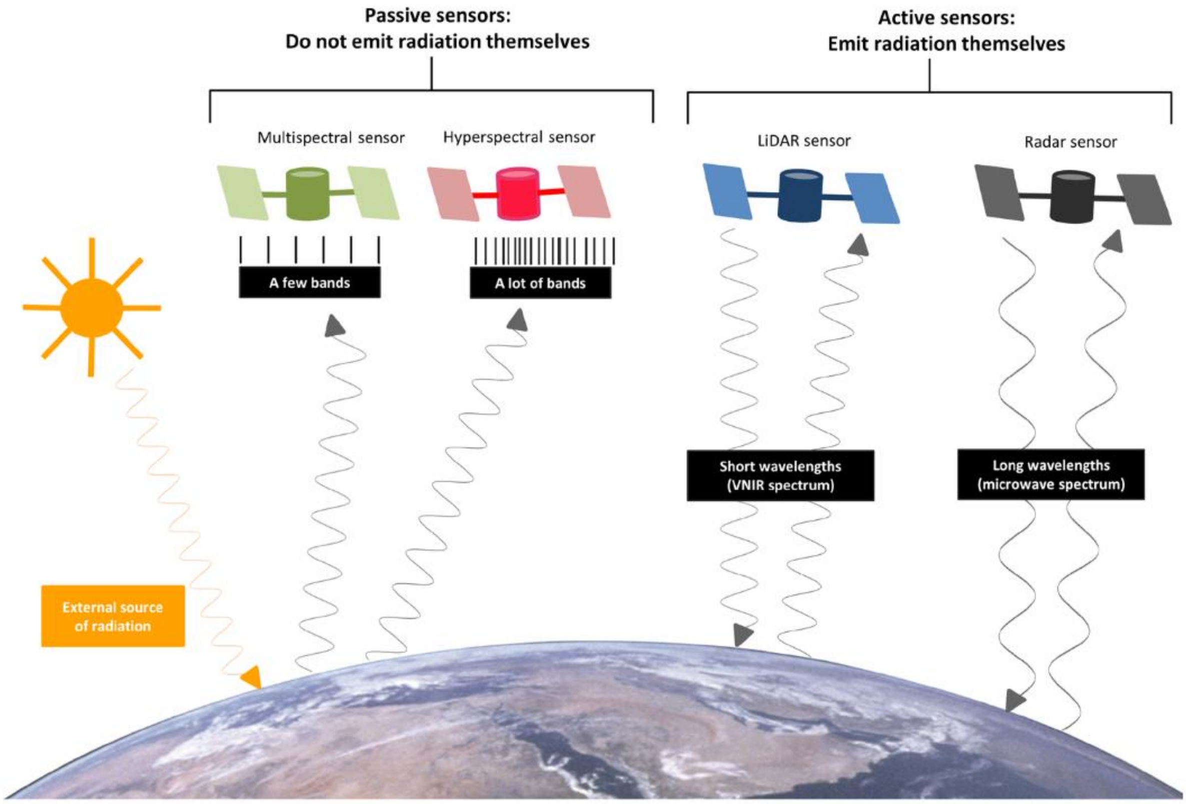

Figure 1: Differentiation between the major types of sensors used in remote sensing. (Pettorelli et al. 2018)

2.1.2 Sensor Platforms

Remote sensors may be mounted to a wide range of platforms, including space-based satellites, manned or unmanned aircrafts, a variety of drones also known as unmanned aerial vehicles (UAVs) or unmanned aerial systems (UASs) and even ground-based systems for field observations. Each platform has different benefits and limitations and therefore advantages and disadvantages. In general, the operating height is directly related to the ground coverage as shown in Figure 2.

Space-based sensors provide large areas within single images and often have long time series of historical data. Satellites with moderate spatial resolution ranging from 10 to 30 meters per pixel in their spectral bands (like Sentinel-2, SPOT-5 or LANDSAT) are freely available while satellites with hight spatial resolution ranging from 1.38 to 4 meters per pixel (like GeoEye-1, WordView or IKONOS) are highly expensive. Satellites have different but fixed revisit times and their data therefore has different temporal resolution ranging from daily up to weekly or even more. The most common limitation of satellite imagery is that cloud coverage can prevent from useful data collection and the images may have to be sorted out. Aerial sensors can be mounted on manned aircrafts like rotary wing helicopters or fixed wing aeroplanes as well on unmanned airships or other remote controlled high-altitude platforms. One benefit of airborne systems is that sensors are exchangeable and different sensors can be combined. Compared to satellites imagery airborne data may have higher spatial resolution and more flexibility in terms of acquisition. On the other hand, the availability depends on weather conditions and the acquisition is relatively expensive. (Chang and Clay 2016)

In recent years the field of remote sensing has been revolutionizied by the emergance of UAVs. Their ability to acquire high to very high-resolution data at relatively low cost equipped researchers with an unprecedented flexibility in data collection and has bridged the gap between field observation and conventional airborne or spaceborne remote sensing. UAVs can be deployed on-demand and can collect data under cloudy conditions thus critical events can be recorded in almost real time. Compared to ground-based field measurements, UAVs enable safe data collection in potentially hazardous and inaccessible areas. These benefits make UAV data indispensable in various applications, such as precision agriculture, environmental monitoring or

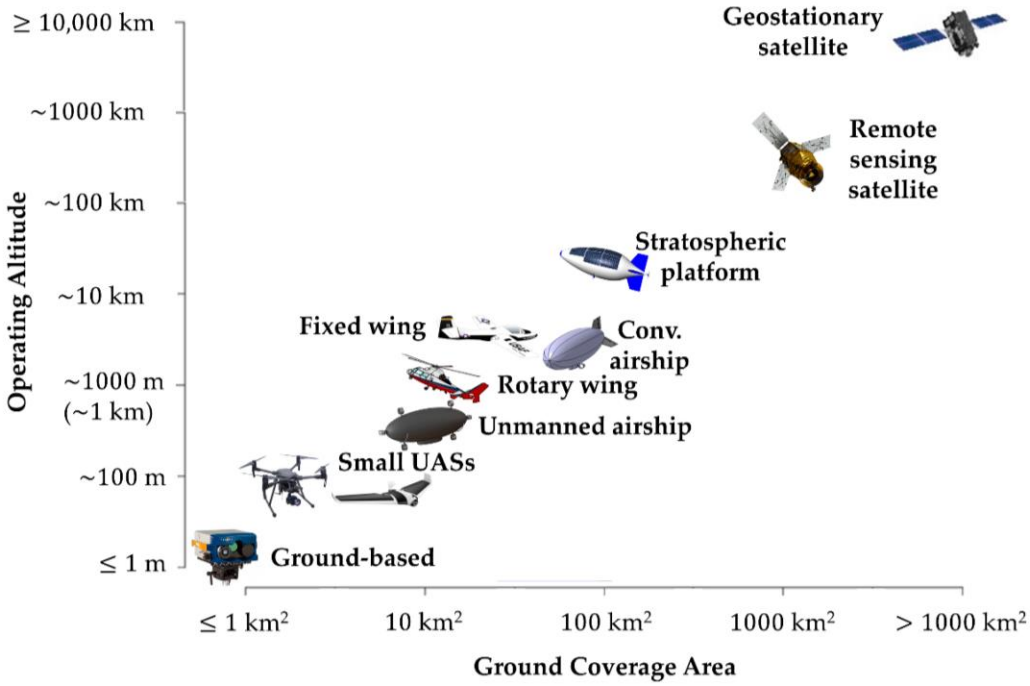

Figure 2: Remote sensing platforms with operating altitudes and respective ground coverage. (Gili et al. 2021)

infrastructure inspection. Although UAVs can reach altitudes of up to 400 metres, their ground coverage is still relatively low compared to conventional remote sensing platforms at medium to high altitudes and is usually limited by battery capacity. Furthermore, additional expertise is required to operate a UAV and process the collected data before further analysis can be carried out. (Manfreda et al. 2018)

2.2 Structure from Motion - Photogrammetry

Remote sensing and photogrammetry are strongly intertwined. While remote sensing involves the recording of aerial images, photogrammetry is concerned with their analysis. Photogrammetry is the science and technology of precisely measuring physical objects based on aerial photographs.

The principal of photogrammetric measurement is the reconstruction of the paths of rays from an area of interest to the sensor of the used camera. While traditional photogrammetric techniques require precise knowledge of the camera location and pose, Structure from Motion (SfM) techniques use algorithms to identify matching features in a set of overlapping digital images (see Figure 3). In this way, camera position and orientation are calculated based on the different position of several matching features which allows the reconstruction of the scene geometry. A set of aerial images received from a flight campaign is stitched to an orthorectified mosaic using image processing methods of SfM photogrammetry. The resulting so called othomosaic is a photographic map with a uniform scale. The spectral signature and structure of different surfaces within the orthomosaic may then be used for classification applications. (Aber et al. 2010)

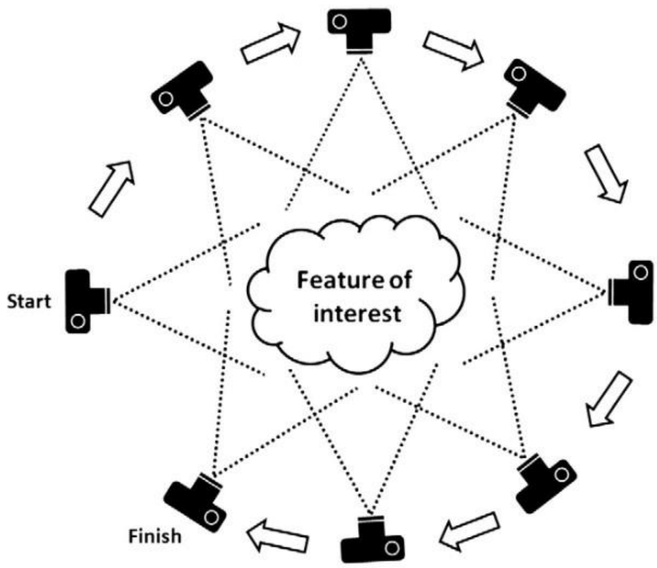

Figure 3: Multiple overlapping photos are required as input for SfM feature extraction and reconstruction algorithms. (Westoby et al. 2012)

The process of generating an orthomosaic is started by loading the whole set of images from a flight campaign into a photogrammetry software. Since modern UAVs usually have internal GPS receiver, the software automatically reads out the geographic information (longitude, latitude, altitude) of each image from its EXIF data. With this information the approximate flight path as well as the approximate location and orientation of the images can be rebuilt. After this first step the initial processing of feature detection (identifying the so called keypoints) is started. Based on this keypoints the different images can be matched and thus the scene geometry can be reconstructed (Carrivick et al. 2016).

After locating the keypoints in each image, correspondences between keypoints in different images need to be determined for images to be matched. The matching keypoints are used to reconstruct the 3D scene structure and calculate the internal and external camera parameters for each captured image during the survey. This processing step is technically known as “SfM” and performed by the software with Automatic Arial Triangulation (AAT) and Bundle Block Adjustment (BBA) algorithms (PIX4D SA 2021a).

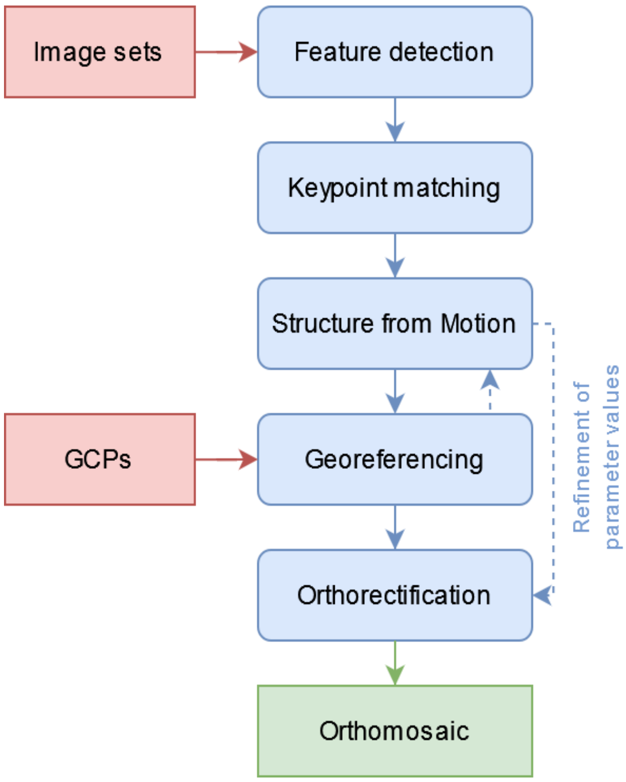

Figure 4: Workflow of generating orthomosaics with SfM photogrammetry methods. (After Carrivick et al. 2016, simplified)

The output of the SfM processing step provides a sparse point cloud with scene geometry and relative camera locations in an arbitrary coordinate system. Since absolute distance between reconstructed points or between cameras cannot be determined from images alone, georeferencing with real coordinates must be applied with a minimum of three ground control points (GCPs) (Szeliski 2011).

GCPs are basically points on the ground with known coordinates that are clearly visible in the captured aerial imagery. Such GCPs may be imported by the photogrammetry software and must be manually located within the arial imagery by the user for georeferencing the point clouds (see Figure 5). Each GCP must be marked on multiple images to ensure high quality of the georeferencing accuracy. With this external information about geolocated GCPs, optimization of image alignment can be achieved by re-running bundle adjustment. This processing step can be seen as a refinement of the parameter values that improves the calibration of the camera parameters as well as the reconstructed scene geometry. (Carrivick et al. 2016)

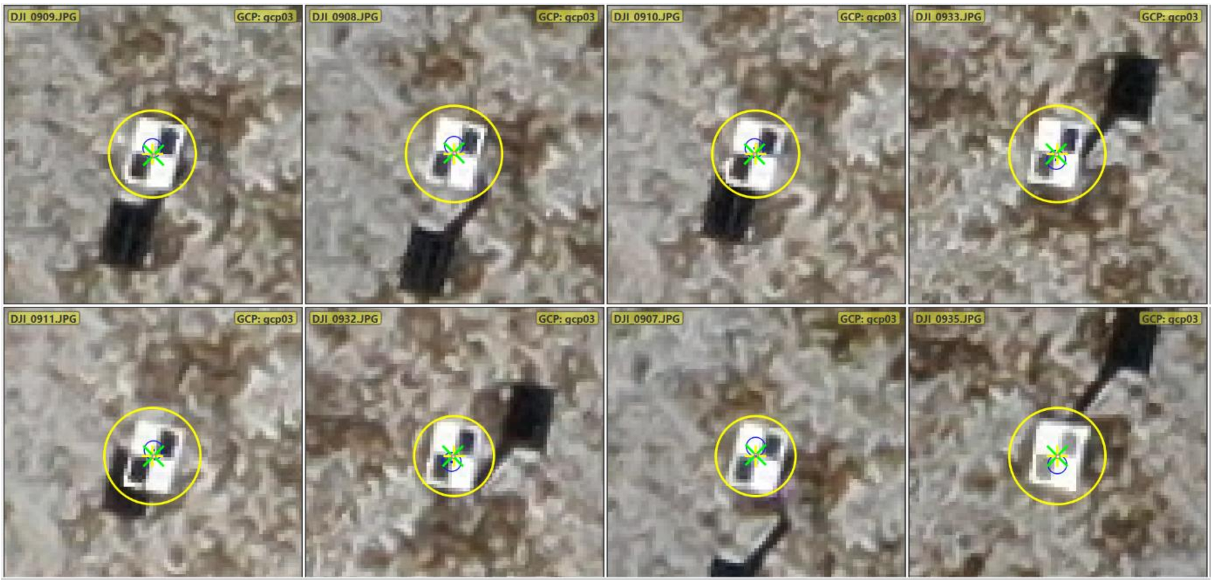

Figure 5: Manual marking of GCPs for georeferencing the point cloud in PIX4d Software.

Once the point cloud is georeferenced and refined a DSM can be derived and an orthomosaic can be generated. The process of generating an orthomosaic is based on orthorectification. With the use of the DSM, the perspective distortions are being removed from the images. The orthomosaic is than generated by projecting the images on a 2.5D model. (PIX4D SA 2021b)

2.3 Image Classification

The term image classification refers to processes for the automatic interpretation of image content. In remote sensing applications, image classification is used to classify land use and land cover by assigning each pixel to a class or to detect features within an image. The task of digital image interpretation or object recognition done by a machine is generally referred to as computer vision. Human performance is enormous when it comes to perceiving image structures, shapes and textures in order to recognise objects, patterns and relationships between them. It long seemed that computers were far from achieving this “typically human” ability. Since the emergence of artificial neural networks, the field of computer vision has significantly developed, as these methods have outperformed traditional machine learning algorithms. However, classification of multispectral data usually involves categorizing the spectral or spatial patterns within the image. Spectral pattern recognition refers to classification procedures utilizing the spectral information of each pixel stored in different bands. Spatial pattern recognition categorizes image pixels in the context with their neighbouring pixels. By considering aspects like texture, pixel proximity and different feature characteristics like shape, size, repetition and directionality, these spatial classification procedures attempt to mimic human like analysis. While traditional machine learning methods mainly concentrate on spectral pattern recognition, modern deep learning approaches work strongly with spatial pattern recognition. In subsequent sections, an overview about both traditional classification algorithms as well as state-of-the-art deep learning methods are introduced. (Lillesand and Kiefer 2000)

2.3.1 Machine Learning

Machine learning (ML) can be considered as a subfield of artificial intelligence which refers to any technique enabling computers to imitate human intelligence. In traditional programming, developers write rule-based instructions for a computer to perform tasks, without explicitly learning from data. The purpose of machine learning is to learn from existing data by training predictive models. The methods used in machine learning can be categorized according to the degree to which they require supervision during the training process (see Figure 6). In contrast to supervised learning, unsupervised leaning does not involve any labelled ground truth data. Therefore, unsupervised learning has an exploratory character and is used to examine naturally occurring patterns in the data without pre-existing knowledge of classes. If supervised learning methods are applied the computer gets trained with data that has a corresponding known class label – a so called labelled training data set. The goal of supervised learning is to learn rules and train a model based on the labelled training dataset that can make predictions for data that the model has not seen before.

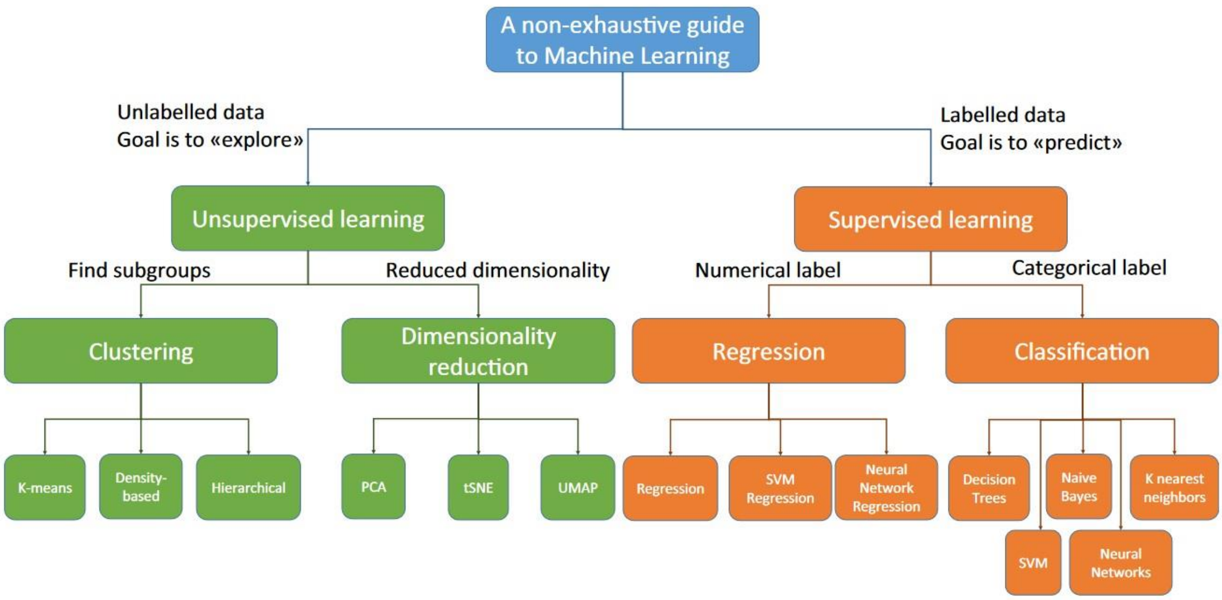

Figure 6: Overview and categorisation of machine learning algorithms. (Badillo et al. 2020)

There is a wide range of algorithms available to be used for machine learning applications. The most popular algorithms used in machine learning are linear regression, decision trees, k-nearest neighbors, principal component analyses, random forest, support vector machine and deep neural networks. Algorithms used in unsupervised learning perform clustering or reduce dimensionality to find subgroups in the data. Algorithms used in supervised learning perform regression or classification to predict numerical or categorial labels. (Badillo et al. 2020)

2.3.2 Supervised model training and assessment

The concept of supervised machine learning is based on training a model with labelled training data. The aim of training is to develop a model that accurately describes the training dataset and is at the same time able to classify independent data without under- or overfitting. To achieve this objective, the model's performance can be evaluated using various methods of model assessment.

The general principle for training and assessing supervised learning models is to divide the labelled dataset into subsets for training and testing (see Figure 7). For each run during model training, the training set is again divided into a different subset of training folds and test folds for

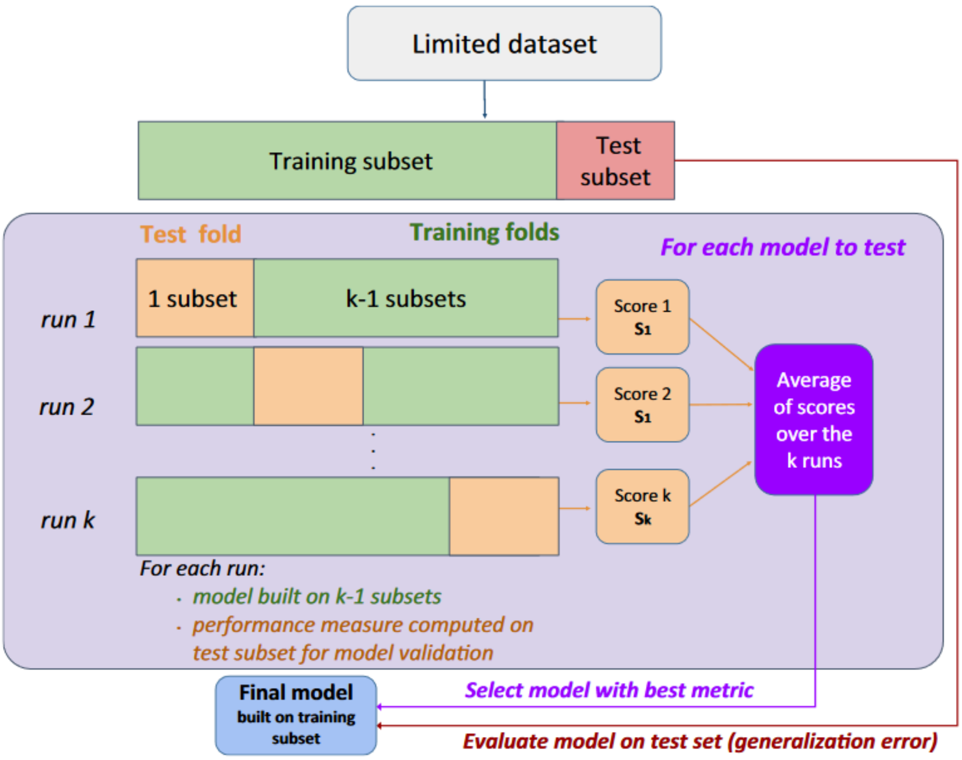

Figure 7: The general principle of supervised learning model training and assessment by dividing the labelled dataset into training, validation and test set. (Badillo et al. 2020)

validation. While the training fold is used to build up the model, the test fold is used to validate the model to derive the best parameter values for training. In the final step, the test set is used to determine the generalization error of the trained model by evaluating the predictive performance of the model when applied to independent data. (Badillo et al. 2020)

During the training process model fitting is done by calculating a loss function that measures the distance between the trained model and validation data. Underfitting occurs when the model's prediction is far from the training set, for example if it is too simple to meet its complexity (see Figure 8, left panel). Overfitting occurs when a model predicts well on the validation set, but poorly on the independent test data set (see Figure 8, right panel). The best fit is found when the model can predict values close to the validation data as well as beyond the training data. (Badillo et al. 2020)

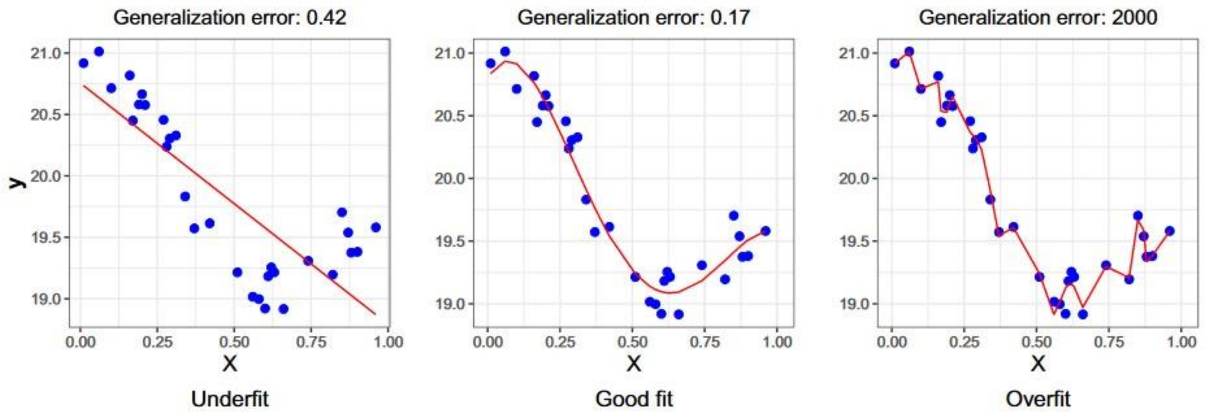

Figure 8: Illustration of model fitting results visualised through a regression. Blue points indicate the training data set and red line indicate the model. (Badillo et al. 2020)

2.3.3 Deep Learning

Deep Learning (DL) can be considered as a subfield of machine learning which involves artificial neural networks. The architecture of an artificial neural network is inspired by the biological structure and function of neural networks in human brains. While the human nervous system consists of cells and synapses, its artificial counterparts are made up of computational units called neurons, which are connected to each other by weights (see Figure 9a). A function is calculated for each neuron, which is influenced by its input weight. This function passes on the values of the input neurons to the output neurons. An artificial neural network learns by changing the weights of the input neurons, when passing it on. The labelled training data provides feedback to check if the weights are correct or if they need to be adjusted to improve the predictions in future iterations.

The simplest neural network consists of a single input layer, weights and an output neuron and is referred to as perceptron. (Aggarwal 2018)

A multilayer neural network contains various computational layers in which the neurons are arranged (see Figure 9b). The input is separated from the output layer by various hidden layers which are not visible to the user. An architecture in which a layer feeds information directly forwards into the next one is also called feed-forward neural network. The term deep learning refers to the depth of such multilayer neural networks meaning the large number of hidden layers between input and output. The accuracy of deep learning models usually outperforms traditional machine learning methods as the amount of data increases, but training such models is computationally intensive. With the increase in data availability and computing power of graphics processing units (GPUs) in recent years, deep learning has gained significant importance in various fields such as computer vision, language translation, medical diagnosis and autonomous vehicles. (Baduge et al. 2022)

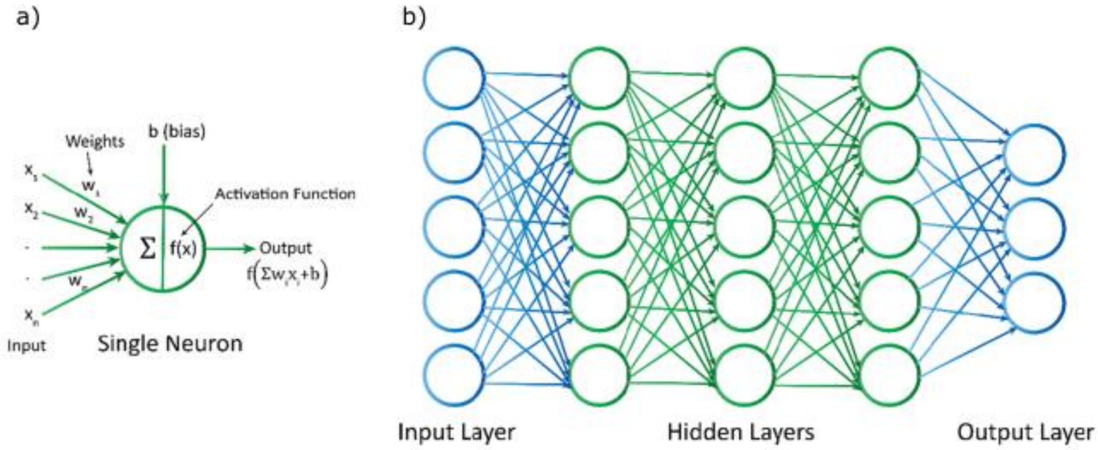

Figure 9: Basic architecture of a perceptron (a) and a multilayer neural network (b). (Baduge et al.2022)

A specific type of deep learning network are convolutional neural networks (CNNs), which are widely used for object recognition and image classification in the field of computer vision. This kind of network can process grid-structured data like remote sensing images. The architecture of a convolutional neural network consists of alternating convolution and pooling layers followed by a fully connected layer (see Figure 10). During the convolution operation a filter (also called kernel) passes through each possible position of the source image or hidden layer and produces a so-called dot product. The result of this process is referred to as feature map and after the convolution process an activation function is applied to the layer. The convolution process is followed by a pooling operation which aims to reduce the dimensions of the previous layer by down sampling. At the end of the network there is a fully connected layer which is connected to the layers produced while feature learning. Parameters like filter size, padding and stride define the architecture of the convolutional neural network. The most popular convolutional networks are ResNet, AlexNet and VGGNet. (Baduge et al. 2022)

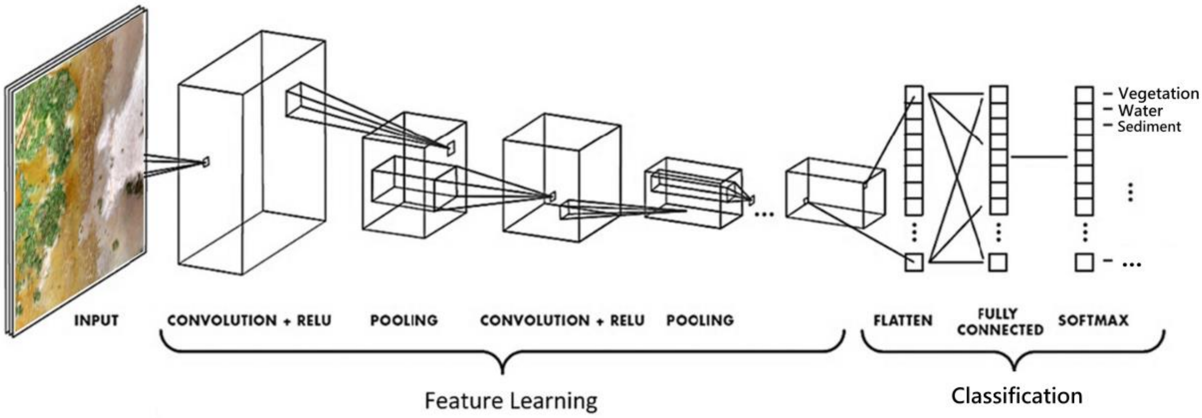

Figure 10: Typical architecture of a convolutional neural network. (Tabian et al. 2019, adapted)

3 Materials and Methods

3.1 Study Area

The study area is located in the reed belt of Lake Neusiedl near Illmitz in Austria (47°46'09''N, 16°45'30''E). With a maximum area of 315 km², Lake Neusiedl is Austria's largest lake, stretching across the Austrian-Hungarian border. It is characterised by a remarkably shallow lake basin (Z_{mean} = 1.2 m, Z_{max} = 1.8 m) with no natural outflow (Wolfram et al. 2013). The lake water has an alkaline and subsaline character (Hammer 1986), with high electrical conductivity (1300-3200 µS cm^{-1}) and an average pH of 8.7. The mean annual precipitation sums between 1971 and 2020 measured from eight stations surrounding the lake were 556 mm, and ranged from 353 mm to 833 mm (Hackl et al. 2023). Due to the relatively small catchment area of the lake, rainfall contributes 79% to the total water supply via direct input through the lake surface. The lake's shallowness and expansive water surface area make it particularly sensitive to climatic variations (Soja at al. 2013).

More than half of the lake (about 181 km²) is covered by a reed belt, which consists of a temporally changing mosaic of reeds (*Phragmites australis*), water, and sediment patches. The lake and its reed belt belong to various protected areas, including the Austrian-Hungarian national park Neusiedler See-Seewinkel/Fertő, a Ramsar site and Natura 2000 area.

This study focused on an area of approximately 53 ha in the eastern reed belt of Lake Neusiedl; the study area extends from sparsely vegetated shores (landwards) to densely vegetated areas near the open lake surface. The area surveyed in the UAV flights was about twice the size of the actual study area (as shown in Figure 11) in order to achieve proper rectification and georeferencing results for the aerial images within the study area. The research area is located in the nature zone of the National Park Neusiedler See-Seewinkel, where no management is conducted and access restrictions apply. An Eddy Covariance (EC) tower for measuring greenhouse gas exchange is located in the center of the study area (https://wetlands.univie.ac.at, accessed on 5 August 2023). Several channels lead through the research area and a constructed dam pathway runs through the middle of the study site, crossing the reed belt from the land shore to the open water area.

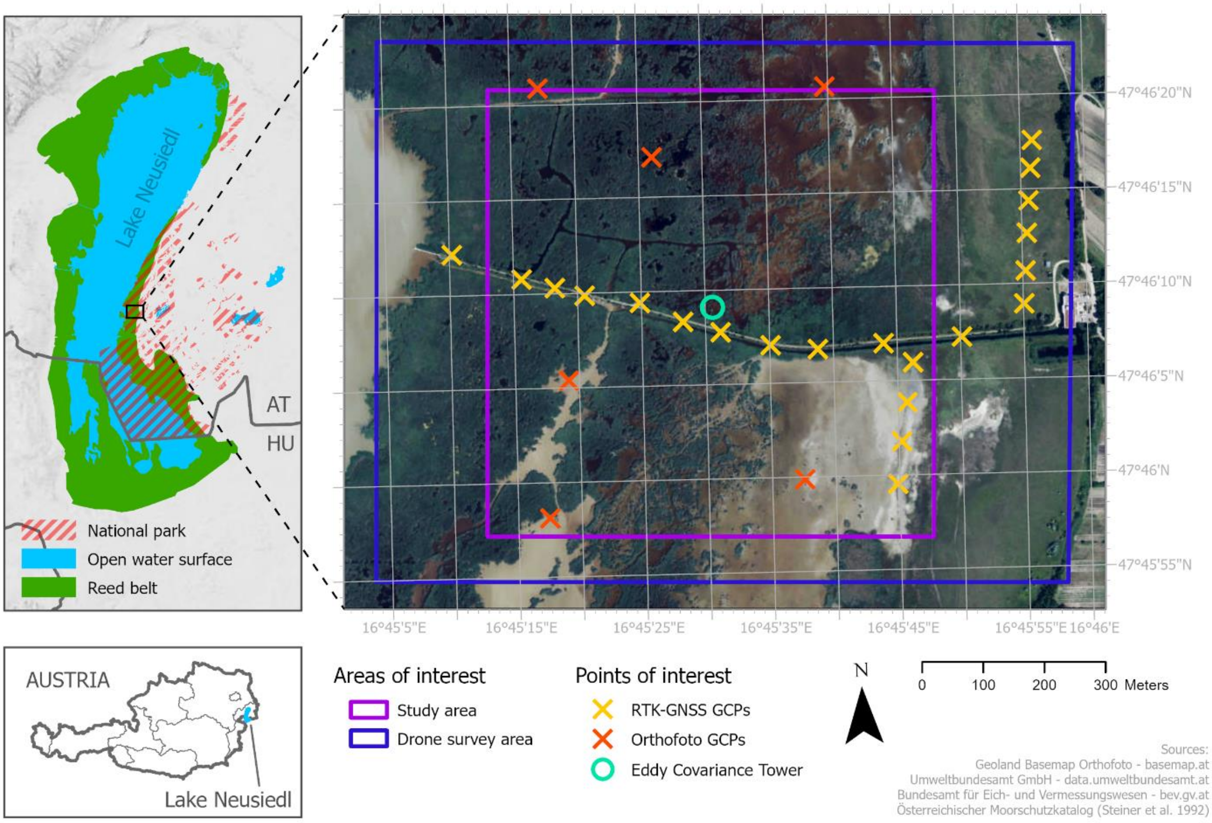

Figure 11. Overview maps and detailed map of the research area in the reed belt of Lake Neusiedl, Eastern Austria (data source used in the overview map: Steiner et al.1992)

3.2 Data Preparation

3.2.1 UAV Data Acquisition

High-resolution images were captured using a quadcopter drone (Mavic 2 Pro, DJI Technologies Co., Ltd., Shenzhen, China) equipped with a CMOS sensor that captures optical images in RGB with a resolution of 5472 x 3648 pixel (20 MP). The camera has a focal length of 10.3 mm and a sensor width of 12.8 mm (DJI 2023). A total of ten flight campaigns were conducted at three-week intervals, starting on 5 May and ending on 6 November 2021 (dates listed in Table 1). Because very few land cover changes in the study area's surface were expected during winter to early spring, no flights were carried out from December to April. The capacity of the four drone batteries covered an average drone survey area of 96 ha during each flight campaign (Table 1), lasting about 2.5 h each. Because distortion can occur at the edges of a processed orthomosaic, we extended the drone survey area well beyond the actual study area used for analysis (see Figure 11). In order to have as little shade as possible in the captured images, all flights were carried out at midday when the sun was at its highest. Because alternating sunny and cloudy weather conditions were to be expected over the duration of a flight campaign, the camera settings (ISO values, shutter speed and aperture) were set to automatic mode during the flights to prevent blurring and/or overexposure in the images. More than 1000 aerial images were generated during each flight campaign, with a mean data volume of 15 GB. All flights were performed in automatic flight mode with predefined parallel flight lines at a constant height of 100 m above the ground and an image front and side overlap of 75%, with all images taken at 90° to the surface (nadir). Flight plans were created using the flight planning app PIX4Dcapture, version 4.10.0 (Pix4D S.A., Prilly, Switzerland).

Table 1. Results and uncertainty values from processing orthomosaics with structure from motion (SfM) techniques.

Flight Campaign	Average GSD [1] [cm]	Drone Survey Area [km²]	RMSE Georeferencing (N = 21)		RMSE Check Points (N = 6)	
			X Error [cm]	Y Error [cm]	X Error [cm]	Y Error [cm]
2021-05-05	2.43	0.84	4.6	2.9	2.0	5.9
2021-05-26	2.39	0.92	23.9	11.7	3.2	3.6
2021-06-18	2.50	1.02	11.6	4.9	1.9	4.4
2021-07-07	2.49	0.99	24.2	8.9	10.7	5.0
2021-07-27	2.45	0.99	14.3	3.0	1.7	4.9
2021-08-18	2.41	0.99	15.5	10.2	3.9	4.2
2021-09-10	2.45	0.95	6.8	3.1	4.5	5.8
2021-09-29	2.36	0.97	5.2	3.8	3.8	5.2
2021-10-20	2.36	0.94	8.3	28.7	2.7	6.0
2021-11-06	2.32	1.00	3.0	1.4	3.2	5.6
Average	2.42	0.96	11.7	7.9	3.8	5.1

[1] Ground sampling distance

3.2.2 Photogrammetric Preprocessing

To georeference the drone imagery, 21 ground control points (GCPs) with a chessboard pattern in DIN-A3 format were produced and distributed in the study area (displayed with a yellow x in Figure 11). To ensure their durability over the duration of all flight campaigns, the GCPs were laminated with a strong and UV-resistant film and fixed to wooden boards before attaching them to driven wooden piles and existing fence posts. Fixing the GCPs on posts above ground guaranteed their visibility to the drone sensors throughout the vegetation period. A GNSS receiver (Trimble R10, Trimble Inc., Sunnyvale, CA, USA) was used for precise location measurement of the GCPs (Trimble 2023). In addition, RTK-based correction using the Austrian Positioning Service (APOS) was applied to improve the precision of the measurements.

To obtain distortion-free image processing results, the GCPs were distributed evenly over the study area (Villanueva et al. 2019). Due to access restrictions in the National Park covering the study area, our original idea of deploying GCPs along the water channels of the study site could not be implemented, as this was considered a potential disturbance factor for breeding birds. For this reason, GCPs were densified along the dam pathway and along the land shore line of the reed belt, where temporary entry was permitted. The area of the drone survey had to be extended in the easterly direction in order to capture the easternmost GCPs with the drone sensor. Furthermore, an additional set of control points (displayed with a red x in Figure 11) was derived from an orthophoto (2019-06-26, resolution 20 cm) obtained from the Austrian Federal Office of Metrology and Surveying (BEV 2023) by manually locating the center of small, isolated, and uniquely identifiable reed patches.

The image datasets from each flight were processed to a rectified and georeferenced orthomosaic using the Structure-from-Motion (SfM) image matching technique, which is widely used in geoscience applications (Westoby et al. 2012) and described in detail by Deliry and Avdan 2021. This preprocessing workflow was carried out using the photogrammetry software PIX4Dmapper, version 4.6.4 (Pix4D S.A., Prilly, Switzerland) according to the instructions (Pix4d Documentation 2023). Processing options such as the image scale at which key points were computed or the degree of camera optimization were adapted to the individual requirements of each flight dataset. In SfM processing, GCPs must be manually marked in different images captured from different angles. Identifying the same geolocation in the small isolated reed patches of the six orthophoto-derived control points was more challenging than identifying the center of the RTK-GNSS measured chessboard-patterned wooden boards designed for accurate marking. Of the 27 available control points, 21 were used for rectifying and georeferencing, while the remaining six served as check points to verify the accuracy of the resulting orthomosaics (results shown in Table 1). The control points derived from the orthophoto were not used as check points, as check points were not included in the process used to rectify the orthomosaic and would have caused wide areas with distortion of unknown extent. The average ground sampling distance (GSD) across all flights was 2.42 cm/pixel. The RMSE (root mean square error) of the control points used for georeferencing was 11.7 cm in the X and 7.9 cm in the Y direction; while relatively high compared to the GSD, this is acceptable considering the size of the covered area. Both the lower resolution of the orthophoto and the inherently less accurate method of identifying the center of the reed patches resulted in significantly higher uncertainty values for georeferencing than we initially aimed for (see Table 1). Because only RTK-GNSS-measured GCPs were used as control points, their significantly lower uncertainty values apply only along the areas of their spatial distribution. The computationally intensive procedure of photogrammetric processing was performed on an Intel(R) Core(TM) i7-10700 CPU @ 2.90 GHz with 32 GB RAM (Intel Corporation, Santa Clara, CA, USA) and a Radeon RX 550X GPU (AMD Inc., Santa Clara, CA, USA).

3.3 Semantic Segmentation

In this study, we used semantic image segmentation for classifying the different land cover types of the study area. Semantic segmentation is a machine learning technique that assigns a class label to each pixel in an image (Shen and Zeng 2019). The whole workflow, from generating training data for deep learning to model training and pixel classification, was carried out in ArcGIS Pro 3.0.3 with the Image Analyst license and Deep Learning Libraries for ArcGIS Pro 3.0.3. Figure 12 illustrates the most important processing steps carried out for each orthomosaic, which are described in detail as follows. (a) Deriving ground truth data: from each orthomosaic, a subset of eight square areas (referred to henceforth as "ground truth areas") covering 2500 m^2 each was obtained. The ground truth areas were carefully selected to cover the various characteristics of the land cover classes, such as their structure and colour expression. Care was taken to ensure that the transition zones between classes (water to sediment, water to vegetation, and sediment to vegetation) were represented within the ground truth imagery. (b) Image annotation: for each of the eight ground truth areas, a fully labeled layer was generated using a semi-automated workflow. A detailed description of the procedure can be found in Section 3.3.1. (c) Construction of a chip dataset for deep learning: a dataset consisting of image chips and analog labels was derived from the fully labeled ground truth data. All chips were exported in TIFF format with a size of 256 x 256 pixels and a 50% overlap both horizontally and vertically. The chip dataset was cleaned to remove chips containing areas without any information. This processing step yielded an average of 1641 chips and the same number of corresponding labels per dataset. (d) Training a deep learning model: the chip dataset was used to train and validate a deep learning model. A detailed description of the procedure can be found in Section 3.3.2. (e) Semantic segmentation for classifying land cover types of the reed belt: the trained model was finally used to assign a semantic class label to each pixel of the respective orthomosaic using the "Classify Pixels Using Deep Learning" tool in ArcGIS Pro. The dam pathway and a boat pier were generously cut out of the classified data used for further analysis.

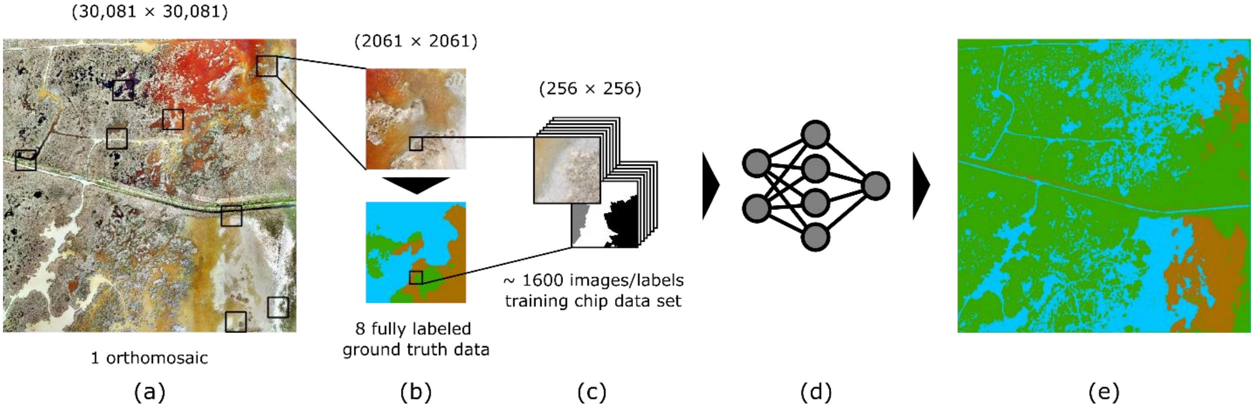

Figure 12. Full workflow for classifying different land cover types in the reed belt through semantic segmentation. The different stages of data processing are shown with the respective image size in pixels. (a) Orthomosaic of the study area (from flight 2021-05-05), with selected locations for ground truth areas. (b) Image annotation data, consisting of ground truth imagery and a fully labeled layer indicating the corresponding land cover classes (vegetation = green, water = blue, sediment = brown). (c) Chip dataset containing small image chips and analog labels derived from ground truth data. (d) Training and validation of a deep learning model with the training chip dataset. (e) Semantic segmentation performed on the orthomosaic using the trained model.

3.3.1 Image Annotation

The process of generating ground truth data is known in the machine learning domain as image annotation. A number of image annotation programs have recently become available, although most of them are proprietary. With the aim of preparing ground truth data at no additional cost and with maximum control over the parameter settings, a standardized semi-automated workflow for image annotation was developed within the ArcGIS Pro environment using the segmentation tool for object based image analysis (OBIA). For each of the ten orthomosaics, a ground truth dataset was prepared as follows (the individual steps are shown in Figure 13):

(a) The eight carefully selected ground truth areas were clipped from the orthomosaic and resampled to a resolution of 10 cm using the bilinear resampling technique. Resizing of the imagery was done to reduce processing time for the next step.

(b) The resampled imagery was segmented into groups of adjacent pixels with similar spectral characteristics. The segmentation tool within the software can be used to define the spectral and spatial detail. It was found that the best segmentation results for distinguishing between the classes in our data were obtained when the spectral detail was set between 15 and 17 and the spatial detail set to 1. Furthermore, the minimum segment size was set to 500 pixels. With these parameter settings, while the segmentation algorithm produced fragmented patches that were smaller then required, it provided proper delineation between land cover classes along certain segment boundaries.

(c) The raster output from the segmentation tool was vectorized for the next processing step.

(d) Segments from the same semantic classes were manually merged. Merging was performed by visual interpretation of the polygons while overlaying the ground truth imagery. To speed up this process, segments smaller than 1 m² were removed and the resulting gaps were filled by adding the geometry of the gap to the adjacent polygon with which it shared the longest edge. This step provided fully overlapping semantic class polygons, with each polygon covering the entire area of a class along with its various intra-class variations contained in the ground truth imagery.

(e) As a last step, the polygons were assigned to the corresponding land cover class in order to obtain a fully labeled polygon layer.

Steps (a) through (e) were repeated for the eight selected ground truth areas from each of the ten orthomosaics. The ground truth imagery in original resolution and the corresponding fully labeled polygon layer were used as input data for exporting the training chips dataset.

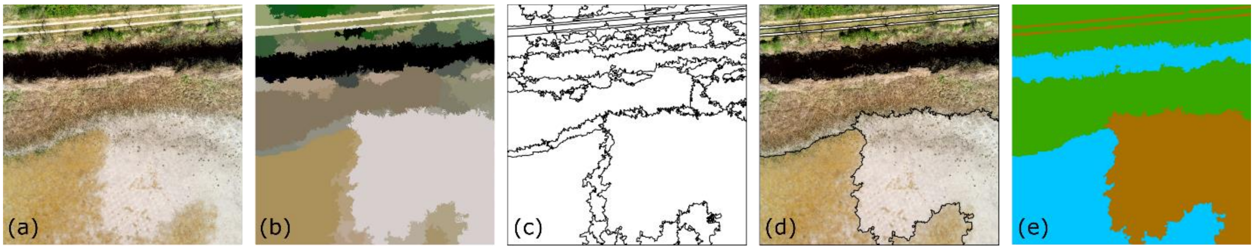

Figure 13. Workflow example of image annotation from one selected ground truth area. (a) Clipped and resampled ground truth imagery covering various characteristics of vegetation, water and sediment. (b) Segmentation output showing adjacent pixel groups with similar levels of spectral detail. (c) Segmentation raster converted into polygons. (d) Polygon segments merged by visual interpretation. (e) Fully labeled polygon layer for respective ground truth imagery, showing the land cover classes of vegetation (green), water (blue), and sediment (brown).

3.3.2 Deep Learning

A deep learning model was trained with each chip dataset using a deep convolutional neural network (CNN) architecture for image segmentation. With the rise of deep learning, CNNs have been applied for various land cover classification applications on high-resolution remote sensing data (Tong et al. 2020, Zhang et al. 2020, Volpi and Tuia 2017). In this study, we used the state-of-the-art DeepLabv3+ model architecture, which uses an encoder-decoder framework with atrous convolution and a variant of the Xception network as its backbone (Chen et al. 2018). This model proved to be highly accurate in wetland classification on high-resolution RGB imagery (Zhao and Du 2016, Pashaei et al. 2020).

The chip datasets were split into 80% training and 20% validation data and stratified in order to maintain the class proportions between the training and validation data. The optimum learning rate for the model training was determined for each chip dataset (see Appendix A). Pre-testing revealed that the model's accuracy was saturated after 20 to 30 epochs. With the intent of making the results more comparable, we trained each model for 25 epochs. Several performance metrics were calculated at the land cover class level to evaluate the accuracy of the models. Precision (1), Recall (2), and F1-Score (3) were calculated as standard evaluation metrics for machine learning models. In addition, Intersection over Union (IoU), which is a standard measure for semantic image segmentation, was calculated using Equation (4) (Rahman and Wang 2016). In contrast to the other metrics, IoU uses the entire ground truth map instead of labeled points to assess the similarity between the predicted and the ground truth map for a given class. This performance metric is progressively being applied in deep learning-based UAV remote sensing classification (Zhang et al. 2020, Pashaei et al. 2020, Zheng et al. 2022, Anagnostis et al. 2021).

Formulas for the above-mentioned metrics are provided in Equations (1)-(4), where true positive (*TP*) represents the count of correctly labeled pixels, false positive (*FP*) refers to the count of pixels misclassified as the target class while belonging to other classes, and false negative (*FN*) refers to the count of pixels that belong to the target class and are misclassified as belonging to other classes.

Equation (1)
$$Precision = \frac{TP}{TP + FP}$$

Equation (2)
$$Recall = \frac{TP}{TP + FN}$$

Equation (3)
$$F1 - Score = 2 * \frac{(Precision * Recall)}{(Precision + Recall)}$$

Equation (4)
$$IoU = \frac{TP}{FP + TP + FN}$$

Model training was carried out on an ArcGIS Notebook (integrated Jupyter Notebook, version 5.7.10) with the *arcgis.learn* module included in ArcGIS API for (Python) 3.9.11. The training took about one hour per model and was performed on an Intel(R) UHD Graphics 630 GPU (Intel

Corporation, Santa Clara, CA, USA) with NVIDIA Quadro T2000 (Nvidia Corporation, Santa Clara, CA, USA).

3.4 Phenological Analysis

A vegetation index was calculated with the aim of tracking phenological stages over the vegetation period within the study area. We extracted the vegetated areas of each orthomosaic using the results from the land cover classification. For these areas, the Green Chromatic Coordinates (GCC) vegetation index was calculated from the red-green-blue (RGB) colour channel information using the formula in Equation (5). Of the various vegetation indices available for RGB data, we chose (GCC) due to its effectiveness in suppressing changes in scene illumination (Sonnentag et al. 2012), which occurred in several orthomosaics.

Equation (5)

$$GCC = \frac{G}{R + G + B}$$

3.4.1 Phenocam Data

In the center of the study area, a digital camera (Powershot SX620 HS, Canon Inc., Tokyo, Japan) was positioned at the Eddy Covariance tower (see Figure 11) in the main wind direction (northwest) to study the phenological changes of the reed plant *Phragmites australis* since September 2020. The Phenocam automatically takes an RGB image every 1 h from 6 am to 5 pm (time zone UTC + 1), which was ensured by manipulation with the Canon Hack Development Kit (CHDK). The photos were analyzed with the R package *Phenopix* (Filippa et al. 2020). For this study, one polygon as region of interest (ROI) was drawn in the reference picture to study the temporal changes of *P. australis* in the entire year 2021 (see Figure 14). For the ROI, the GCC vegetation index was extracted using an ROI-averaging approach (Filippa et al. 2016). GCC values were filtered according to the *max* approach following Sonnentag et al. 2012 after determination of the 90th percentile values in three-day moving windows, as this filter effectively minimized the impact of lighting changes in the environment.

Processing and statistical analysis of the Phenocam data were carried out using R (Version 4.1.2, (R Core Team 2022). For faster data processing, the R package *data.table* was used (Dowle and Srinivasan 2023). The R package *ggplot2* was used to visualize the results (Wickham 2016).

Figure 14: The region of interest (ROI) is marked as a black polygon in the reference picture 2021-06-23 of the Phenocam, which is aligned at the Eddy Covariance tower in the reed belt of Lake Neusiedl in the main northwest wind direction.

4 Results

4.1 Performance Metrics

Performance evaluation of deep learning models was based on the accuracy metrics Precision, Recall, F1-Score, and IoU. The Precision, Recall, and F1-score achieved mean results above 90% over all class types, with a small deviation in the maximum SD of 2.7% (see Table 2). The vegetation class scored particularly highly on these metrics, with noticeably low deviation. The IoU reached mean results ranging from 68.5% to 89.9%, showing higher variance within the class types. The vegetation class again performed the best of all classes. The sediment class type achieved a mean IoU of 72.0% with an SD of 8.1%, and the water class type reached a mean value of 68.5% with a comparably high variance of 11.5% SD. Detailed information on the models' accuracy metrics can be found in Appendix A.

Table 2. Performance metrics of deep learning models (N=10) trained for land cover classification of UAV[1] imagery tracking the reed ecosystem from May-November 2021. Metrics are represented with mean values ± SD[2] of trained models at the class level. The full table is provided in Appendix A.

Class	Precision	Recall	F1-Score	IoU [3]
	Mean ± SD	Mean ± SD	Mean ± SD	Mean ± SD
Vegetation	0.958 ± 0.010	0.957 ± 0.007	0.958 ± 0.006	0.899 ± 0.020
Water	0.929 ± 0.026	0.923 ± 0.024	0.925 ± 0.020	0.685 ± 0.115
Sediment	0.918 ± 0.023	0.927 ± 0.027	0.922 ± 0.020	0.720 ± 0.081

[1] Unmanned Aerial Vehicle, [2] Standard Deviation, [3] Intersection over Union.

4.2 Land Cover Classification

From each orthomosaic (N=10) area shares of the three land cover class were calculated. Figure 15 shows the spatial and temporal variability of land cover in the study area within the study period of May to November 2021.

The majority of the study area is covered with vegetation (60.8% to 70.9%), and vegetation has the lowest variation of all the class types over the entire study period. The vegetated area showed a rapid increase from May to mid June (+6.6%). After a sudden vegetation decline at the beginning of July (-2.7%), a steady increase began, peaking at the end of September (+6.2%). Thereafter, the vegetation class remained almost stable, with a slight decline until November (-0.3%). The area shares of water and sediment have an interdependent relationship, and show similar variations, although their area shares differ. Water had its maximum surface coverage in May (29.9% and 30.2%), when sediment showed its minimum extent (9.3% and 6.3%). Within two months, a strong decline in the water class (-25.2%) caused sediment to reach its maximum extent (29.4%) at the end of July. In August, the water area increased slightly before declining to its minimum extent at the beginning of September (3.3%). From the end of September to November, the respective shares of water and sediment areas fluctuated at a very low level, with maxima of ±0.5% and ±0.7%, respectively.

The changes in the spatial distribution of land cover classes during the study period are shown in the land cover classification maps in Appendix B. An increase in vegetation area was observed along the edges of existing reed stands. For this reason, the water channels became increasingly overgrown with *Phragmites australis* during the study period, as can be seen in the maps. In addition, densification of loosely vegetated areas was observed from early May to late September. The land cover development in the study area shows a constant and large increase in sediment area from the land shore side combined with a large decrease in water area from end of May to end of July 2021. Moreover, the maps show a rather stable spatial distribution with minimal changes in land cover from the end of September to the beginning of November.

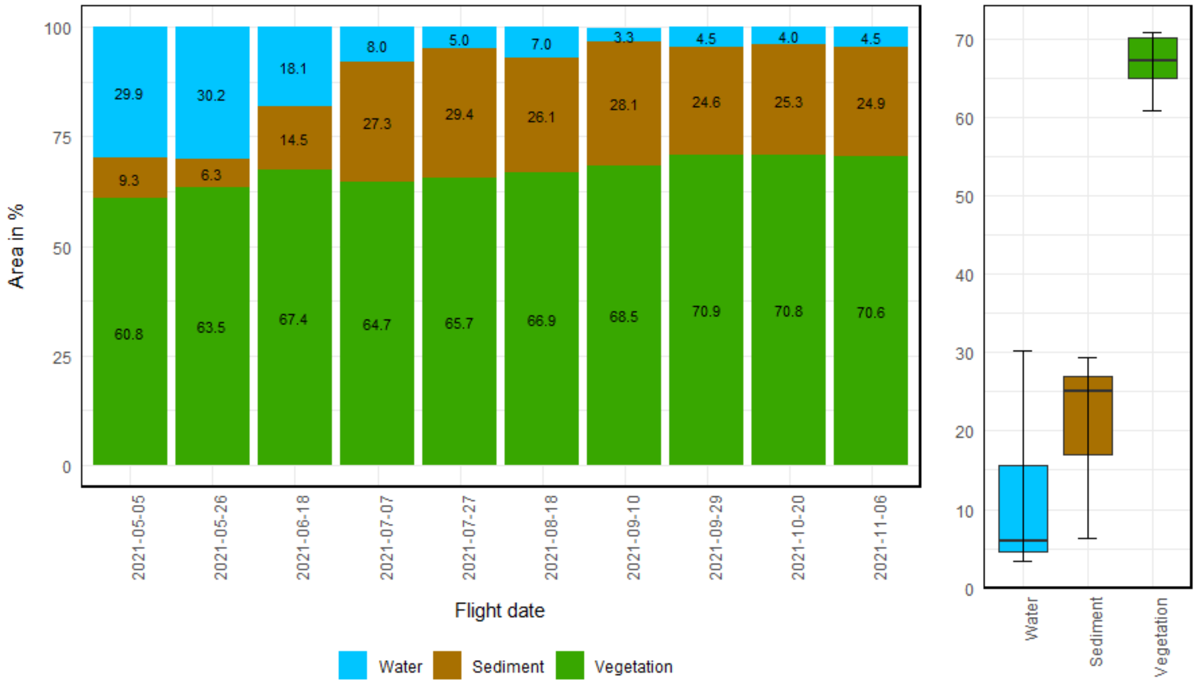

Figure 15. Spatio-temporal variability in the study area of Lake Neusiedl's reed belt from May-November 2021.

4.3 Vegetation Index

The seasonal course of vegetation development during the study period could be observed based on the orthomosaics of our study area. For better understanding of phenological development, GCC values were calculated for each pixel of the vegetated areas. The seasonal course of vegetation phenology in the entire vegetated study area is presented as the mean ± SD of the GCC value pixel counts, and can be seen in green in Figure 16. In the study period, the mean values of GCC ranged between 0.33 to 0.40. The vegetation areas showed an increase in GCC values from early May until late July, when it peaked. Thereafter, the mean GCC values decreased and remained stable at 0.37 until the end of September, continuing to decrease until again reaching the baseline value from early May (0.33) in November.

The GCC maps in Appendix B reveal the spatial and temporal heterogeneity of the phenological development within the vegetated areas. At the beginning of the study period, the GCC values increased along the edges of existing reed stands and in loosely vegetated areas. In areas of dense vegetation, the GCC values gradually increased until the end of July, though they did not reach the maximum in the most densely vegetated areas. The GCC histograms in Appendix B differ in width and height. A narrow distribution of GCC values indicates more homogeneous status of the reed stands (e.g., 2021-05-05), while a wider distribution shows heterogeneity of reed shoot development within the reed stands (e.g., 2021-07-27).

The Phenocam provided us with the opportunity to study the phenological changes of the reed stands of *P. australis* to the northwest (the main wind direction) of the EC tower located in the center of the study area on a daily basis. The trend of the GCC values of the Phenocam in 2021 are shown together with the mean ± SD GCC values of the UAV flights in Figure 15. From January to the beginning of May, the GCC values of the Phenocam were stable at 0.33 (phenology stage *Dormancy*). The GCC values started to increase in the beginning of May 2021 (DOY 124). The phenology stage *Greenup* ranged until the beginning of June (DOY 159). The phenology stage *Maturity* started at DOY 160, with the highest peak at the beginning of July (DOY 177) with 0.42. The *Senescence* phenology stage started at the beginning of August (DOY 213). The GCC values decreased to 0.33 until the end of October (DOY 298), then slightly increased in the *Dormancy* phenology stage to 0.34 at the end of the year 2021. According to the GCC values of the Phenocam data, the vegetation period of the reed stands next to the EC tower in 2021 was around 173 days (4 May until 24 October).

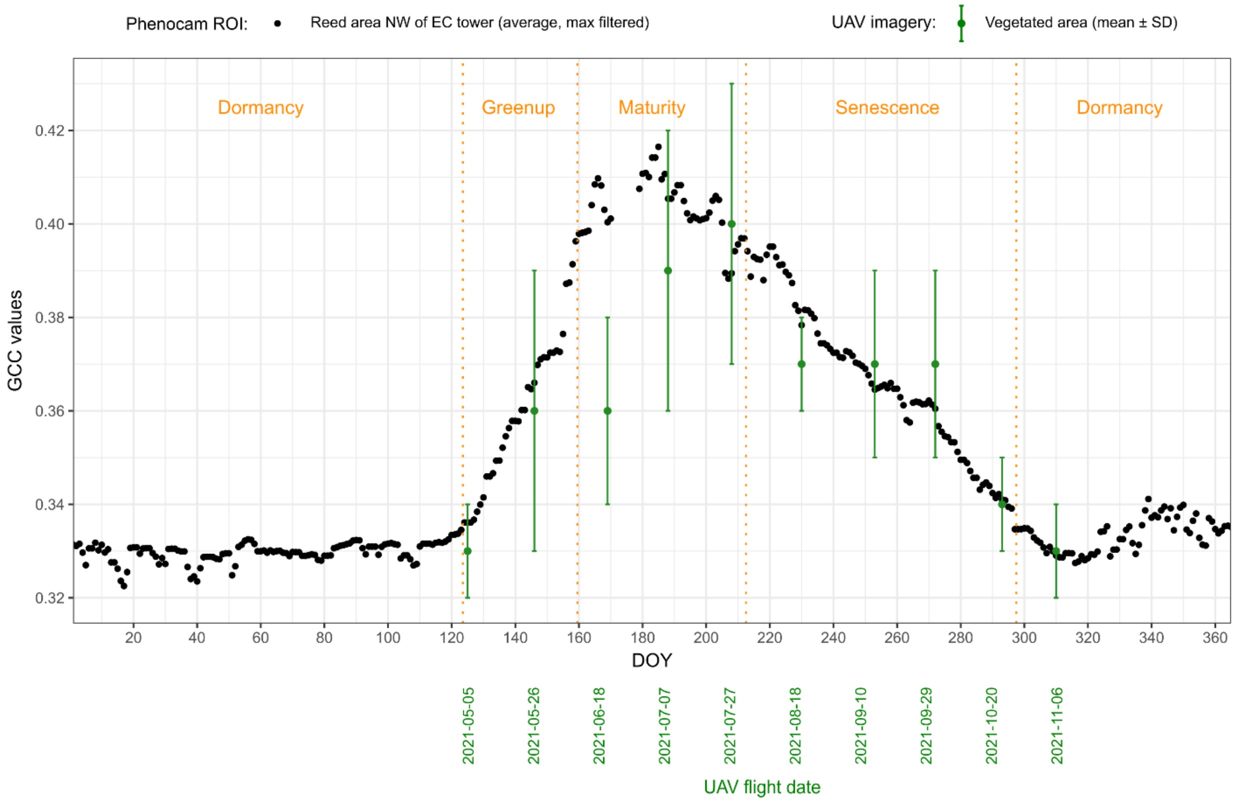

Figure 16. Comparison of the seasonal course of vegetation phenology (year 2021) between the ROI of the phenocam data and the study area covered by the UAV imagery using the GCC vegetation index. The GCC values of the Phenocam ROI (black dots) show the average phenology of the reed stands at the Eddy Covariance tower in the NW direction (center of the study site) for almost every day of year (DOY) in 2021 as compared to the mean ± Standard Deviation (SD) of the GCC values calculated from the ten UAV flights (green dots with error bar) for the entire study site covering the land to the open water shore of the reed belt. The phenology stages of the Phenocam data are separated by the orange dotted lines.

5 Discussion

Changes in the land cover and phenological stages of the reed belt of Lake Neusiedl were investigated and identified using ten study dates in the period between 5 May 2021 and 6 November 2021. Land cover classification was performed using deep learning image segmentation, while phenological analysis were carried out using the GCC vegetation index. As a basis for these analyses, SfM-derived orthomosaics generated with high-resolution RGB drone imagery were used. Furthermore, we have provided the detailed workflow used in generating the fully labeled ground truth data for training and validation of our deep learning model.

Due to access restrictions, GCPs could not be evenly distributed within the study area as recommended (Villanueva and Blanco 2019). In order to obtain comparable SfM results and derived subsequent land cover classifications, it was necessary to acquire additional control points from an orthophoto. This solution led to a higher RMSE than was initially targeted in terms the uncertainty values of the SfM processing; however, this was accepted due to the lack of alternatives and can be considered sufficient as compared to the existing literature (Deliry and Avdan 2021). Considering the access restrictions imposed by the National Park, the minimally invasive method of UAV surveying is currently the most feasible way to collect data covering large areas with this level of detail, despite the constraints around GCP distribution.

One of the biggest challenges anticipated in our study involved the different appearance of the surface of the study area throughout the investigation period due differences in the sunlight conditions between flights. As can be seen from Figure 13 and Appendix A, even within a single orthomosaic the study area showed strong variations within classes; e.g., water could range from crystal-clear to opaque turbid due to the sediment load, and had different color expressions, while certain inter-class expressions such as dry sediment and dead reeds hardly differed. Our attempt to use traditional machine learning techniques, namely, Support Vector Machine and Random Forest, delivered strong pixel misclassifications due to the above-mentioned challenges. The use of deep learning for image classification considerably reduced this kind of misclassification error; however, our attempt to train a single deep learning model using the training chips from the flight campaigns during which the reeds were in the phenological maturity stage in order to classify the corresponding orthomosaics using the same generic model was unsuccessful. Not only were the performance metrics significantly lower for this model, the classification results were weak. Strong noise occurred in certain areas, described as “pepper effects” by Zheng et al. 2022. Large areas of changing light conditions were generally misclassified, and transition areas between land cover classes appeared in straight edges rather than smooth lines. As a consequence, we trained an individual model for each orthomosaic. This approach, described in Section 4.1, achieved satisfactory results in terms of performance metrics compared to related studies (Zheng et al. 2022, Al-Najjar et al. 2019, Bhatnagar et al. 2020). The individual models were good at merging intra-class variation into one class as well as at distinguishing between classes. Even changes in the light intensity of the images due to changing sunlight conditions, which the authors of Bhatnagar et al. 2020 stated as a key challenge, did not influence the classification results of the affected orthomosaics.

While reed ecosystems such as the reed belt of Lake Neusiedl are very valuable wetlands for nature conservation, they are difficult to access and should generally not be entered; remote sensing is an excellent tool to circumvent these concerns. As such, UAV data were used to determine the height, status, and density of reed stands in the lake (Meneses et al. 2018a, Meneses et al. 2018b). Other studies have mostly used satellite data to separate reed beds from other vegetation in wetlands (see, e.g., Villa et al. 2013, Davranche et al. 2010), while other studies have used airborne laser scanning to map the extent of reed wetlands (see, e.g., Csaplovics and Schmit 2011, Márkus and Király 2012, Zlinszky 2013, Dienst et al. 2004). These studies investigated the respective reed ecosystems only once in a growing season. In addition, airborne laser scanning is highly costly compared to using a UAV. There have been studies mapping salt marshes, including reed ecosystems, with satellite data along the coast and comparing the classification results between the years; see, e.g., Sun et al. 2023. The evaluation of reed bed changes in Tiškus et al. 2023 showed that changes were induced by management, i.e., reed mowing. In general, satellite data offer lower resolution, and can involve difficulties with cloud cover compared to remote sensing via drone. The height and greenness of vegetation in a floodplain partly covered with reed was studied with several UAV flights per year in van Iersel et al. 2018. Higgisson et al. 2021 illustrated that the structure of the reeds was detectable by a CNN. Our study showed that drone (UAV) remote sensing combined with deep learning is a powerful tool for surveying and classifying reed beds of wetlands in high detail. High-resolution images were obtained several times within a single growing season, allowing the phenology of the reed plant *Phragmites australis* to be observed. We were able to determine the extent of the reed stands as well as the changes in the surrounding areas, such as water and sediment areas, which were induced by the decrease in the water level of the lake due to drought conditions.

5.1 Model Prediction

As input for model training, we fully labeled a subset of eight square-shaped areas on each orthomosaic using the semi-automated image annotation workflow described in Section 3.3.1. These labeled ground truth areas summed to only 4% of the entire study area, and the model prediction yielded favourable results for land cover classification despite the expected challenges stated above. We assumed that it would be crucial to cover the various expressions of each class in the training data; thus, the selection of training areas was carried out with great care. To assess the quality of the model prediction, we manually labeled a representative test area and compared it with the classification results for the same area. The error map in Figure 17 shows that the differences between model prediction and the labeled test area occurred almost exclusively along the class boundaries, where different reasons for pixel misclassification could be identified.

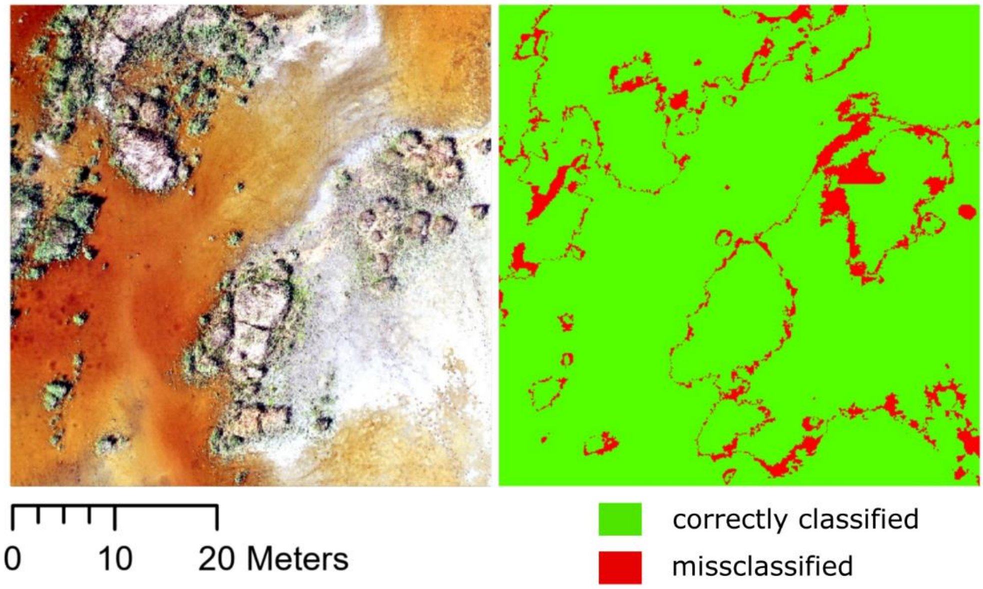

Figure 17. Classification performance of a deep learning model visualized in an error map, showing the difference between labeled test data and the model prediction in a reed ecosystem. Misclassification occurred primarily along class boundaries, especially in transition zones with sparse reed vegetation or very shallow waters, as well as in heavily shaded areas.

First, class boundaries resulting from model prediction ran more smoothly than the class boundaries resulting from the image annotation workflow, which can be considered a negligible error. Second, class boundaries were difficult to predict in extensive transition areas, for example, where water level depths were in the centimeter to millimeter range or in areas with sparse reed vegetation. Third, shaded areas were often reported as misclassified even though they may have been more accurate than the ground truth when compared directly to the imagery. This error may contribute to the significantly lower IoU values for water and sediment in the model performance metrics (see Table 2 and Appendix A), and suggests that preparation of ground truth data must be done with utmost care. Because misclassification occurred primarily along class boundaries, we believe that adding more representative training data from transition zones could further improve model performance. On the other hand, transition zones are inherently difficult to delineate, which poses a challenge when generating training data. Both the OBIA segmentation tool used in this study and the visual interpretation when merging the segmented polygons had limitation in terms of the accuracy of separating classes in the transition zones.

5.2 Spatio-Temporal Variability

The results of the land cover classification show a clear dominance of reed vegetation in the study area. Previous studies showing a decline of aquatic reeds in central Europe during the last decades (Dienst et al. 2004, Nechwatal et al. 2008, Ostendorp 1989) do not match our data within one year. The vegetation area recorded a continuous increase from May to September except for a short period from mid-June to the beginning of July 2021. This rebound of vegetation was likely due to the sudden and complete drying of former water pool areas along the northeastern shore (landward) side of the study area. These pools were sparsely overgrown with juvenile reed shoots in spring, and could be detected well as vegetation by the model. When the pools dried out, increased salinity may have contributed to the dying back of juvenile shoots (Lissner and Schierup 1997), leading to leaf area loss until the plants could no longer be detected as vegetation by the model. It was clear that large water pool areas dried out and became sediment areas during the study period; when the sediment area reached its maximum extent at the end of June, it was more than four times the size of its minimum extent at the end of May. Water areas declined rapidly from the end of May to mid-September, with the exception of a slight increase on 18 August 2021 due to precipitation in the days immediately preceding the UAV flight (about 20 mm (Wasserportal Burgenland 2023). The distribution of area shares hardly changed from the end of September to the end of the study period. The minor decrease in vegetation area within this period suggests that biomass was no longer being built up, reed growth stopped, and reed leaf surfaces shrank slightly due to dehydration and the onset of wilting. Water and sediment areas were stable because water input (precipitation) and evaporation rates were in balance at this time of the year.

The seasonal temporal changes of the water level of Lake Neusiedl and of the reed belt usually occur annually, with a maximum in spring (March/April) and minimum in autumn (September/October) (Hackl ad Ledolter 2023). Therefore, the temporal change of the mosaic of the reed belt consisting of reed stands, water, and open sediment areas occurs annually due to the change in water level even in “normal” years, though of course with a lower extent compared to the results of our study. Because the reed belt has a gradient from land to open water, spatial changes occur at different rates within the reed belt even in “normal” years. Thus, temporal and spatial changes can be observed in “dry” years as well as in “normal” years. Of course, 2021 was an extreme year, with an especially dry autumn, and conditions actually intensified the following year. It may be suspected that a major consequence of the observed changes in “dry” years for the ecosystem of Lake Neusiedl would be a disconnection between reed belt and open water areas, which would alter food webs and have faunistic and biogeochemical consequences, among others. In “wet” years, on the other hand, there would naturally be rather less spreading of the reed stand areas, though water level changes would nevertheless continue over the year. In this context, however, it should be noted that the last “wet” year with high water levels was 2014 (Hackl and Ledolter 2023).

None of the current studies of Lake Neusiedl (Nemeth and Dvorak 2022, Csaplovics 1982, Csaplovics and Schmidt 2011, Nemeth et al. 2014, Csaplovics and Nemeth 2014, Márkus and Király 2012) have investigated the spatial and temporal pattern of the three wetland classes (reed, water, and sediment) within one year, though they have often compared the extent of the reed belt between two years, for example, 1979 and 2008. Our study is the first to identify open sediment areas as a separate land cover class in the reed belt. Comparing August 2008 (Csaplovics and Schmidt 2011) with August 2021 of our study, the share of water areas in the reed belt decreased by 3.7% (from 10.7 to 7%), which would be an opposite development from that of 1979 to 2008, and the vegetation coverage decreased from 88 to 67%. However, Csaplovics and Schmidt 2011 surveyed the entire Austrian reed belt and reported only humic water; therefore, it is unclear whether the lake water of the channels is included in the water areas of the reed belt, as it is not shown as separate class. In contrast to Nemeth and Dvorak 2022, Márkus and Király 2012, Dinka et al. 2010, we observed no die-back sites in our study site for the period from May to November 2021.

The entire lake, including the reed belt, experienced a sharp drop in water level in 2021; thus, the decrease in water areas inside the reed belt could be observed in other parts of the reed belt of Lake Neusiedl as well. Therefore, the decline in water areas in our study can be generalized to an extent to the entire reed belt of Lake Neusiedl. However, because the reed stands vary in age and structure depending on usage/management (west side) or no usage (east side) (see e.g., Csaplovics and Schmidt 2011), and some even include reed stands that have died back (see Nemeth and Dvorak 2022, Dinka et al. 2010), the increase in reed area within the reed belt cannot be generalized to all areas. Nevertheless, this study shows exemplary temporal and spatial changes in the three wetland classes over the 2021 vegetation period, which was affected by drought conditions.

5.3 Vegetation Phenology

Recently, an example of rapid change in wetland vegetation has been reported from the Rodewiese site, a formerly drained fen on the Baltic coast in NE Germany that was rewetted in 2010. Grassland species that are sensitive to a high water table, such as *Holcus lanatus*, *Potentilla anserina*, and *Trifolium repens*, died back very quickly and were replaced by hydrophytes such as *Lemna* spp. and, with some delay, *Bolboschoenus maritimus*, *Schoenoplectus tabermontanii*, and *Phragmites australis* (Koch et al. 2017). Then, in 2018, most of the site that had been covered by water experienced a drought and turned dry, and the fen canopy, with the exception of *Phragmites australis*, disappeared and was colonized by *Tephroseris palustris* and *Ranunculus sceleratus* (Beyer et al. 2021), pioneer species that rapidly spread along nutrient-rich shores of dried-up water bodies (Fukarek e al. 2016). Beyer et al. 2021 have pointed out that analogous climate effect feedback generally cannot be anticipated; moreover, van Diggelen et al. 2006 and Klimkowska et al. 2010 pointed out that in restored fens, water availability, soil, and trophic status were irreversibly altered, along with propagule availability. The conditions experienced in the reed belt of Lake Neusiedl favour *Phragmites australis* as long as the broad ecological amplitude of this reed is not surpassed.

The vegetation in the study area is dominated by reeds, and was tracked using the GCC vegetation index for phenological analysis. The Phenocam data suggest that the phenological time window of the reed stand was well covered in this UAV study. Nevertheless, there is an offset in the GCC data between the Phenocam and the UAV flights in the phenological *Greenup* phase, which is probably due to the different image perspective. Due to the Phenocam's lateral perspective of the reed plants, it naturally detects greening-up earlier than the UAV does from its nadir perspective. However, the UAV covers a much larger spatial area, which of course develops at different rates in the *Greenup* phase from land to open water areas; we have shown the mean and standard deviation of the GCC for the entire study area in Figure 16. The GCC maps in Appendix B show that new vigorous reed shoots grow first along the edges of reed stands and in loosely vegetated areas, leading to an expansion of the vegetation area. In the existing reed mats, shoots break through only gradually, especially in dense areas. When GCC levels peaked in late July, the densest areas of the reed mats were only sparsely overgrown with new reed sprouts; therefore, we do not consider these to be die-back sites.

Phenocam data have the advantages of a lateral perspective and high temporal resolution (hourly/daily basis); however, they are limited to the small area that a single photo is able to cover. On the other hand, while aerial surveys with hundreds of images acquired during a UAV flight campaign can provide detailed information on the spatial development of vegetation over a comparatively large area, they are limited to a lower temporal resolution. Therefore, a combination of both methods can provide complementary analysis.

6 Conclusions

This study aimed to investigate the spatial and temporal changes in the reed belt of Lake Neusiedl under intensive drought conditions. For this purpose, a set of 10 SfM-derived orthomosaics from UAV imagery collected over the 2021 growing season was created. The high-resolution orthomosaics served as a basis to detect changes in land cover and to reveal phenological development. We have demonstrated a semi-automated procedure for generating fully labeled ground truth data for deep learning image segmentation in the context of land cover classification of a wetland. The results of this study underline the strong ability of deep learning models to extract complex features from high-resolution imagery. However, our unsuccessful attempt to train a generic model using training data from multiple flight campaigns encountered limitations. The classification maps revealed an enormous decline in water areas within the reed belt, with a simultaneous increase in sediment areas during the investigation period. Reed vegetation, on the other hand, increased at a nearly constant rate throughout the growing season due to vigorous reed growth along existing reed stands and in loosely vegetated areas, as identified by the GCC maps. While the results of our study can be generalized to the entire reed belt of Lake Neusiedl to a certain extent, the findings may not be applicable to other ecosystems with different environmental factors. This study provides a detailed dataset which can be used to assess the habitat diversity of the reed belt or its ecosystem productivity. In particular, the generated land cover maps may serve as ground truth data for upscaling to more coarsely grained sensor data such as satellite imagery.

Appendix A

Table A1. Detailed table of deep learning parameters and performance metrics. Ten CNN models were trained for land cover classification of UAV imagery for tracking a reed ecosystem over a vegetation period.

				Precision			Recall			F1-Score			IoU		
Orthomosaic Date	**Image Chips Used for Training**	**Learning Rate**	**Accuracy of Last Epoch**	**Vegetation**	**Water**	**Sediment**	**Vegetation**	**Water**	**Sediment**	**Vegetation**	**Water**	**Sediment**	**Vegetation**	**Water**	**Sediment**
2021-05-05	1621	0.0004	0.945	0.958	0.967	0.892	0.941	0.946	0.952	0.950	0.956	0.921	0.851	0.837	0.629
2021-05-26	1642	0.0010	0.948	0.972	0.918	0.927	0.964	0.945	0.908	0.968	0.931	0.918	0.920	0.847	0.575
2021-06-18	1537	0.0010	0.958	0.977	0.959	0.931	0.965	0.917	0.975	0.971	0.938	0.953	0.924	0.731	0.784
2021-07-07	1574	0.0005	0.935	0.960	0.936	0.868	0.955	0.939	0.899	0.958	0.938	0.883	0.910	0.766	0.662
2021-07-27	1696	0.0008	0.939	0.948	0.878	0.944	0.957	0.912	0.924	0.952	0.895	0.934	0.887	0.476	0.801
2021-08-18	1642	0.0008	0.936	0.964	0.908	0.909	0.951	0.867	0.955	0.958	0.887	0.932	0.905	0.639	0.797
2021-09-10	1533	0.0005	0.950	0.951	0.952	0.947	0.964	0.906	0.951	0.958	0.928	0.949	0.890	0.603	0.835
2021-09-29	1706	0.0005	0.937	0.952	0.904	0.931	0.962	0.915	0.906	0.957	0.909	0.918	0.906	0.543	0.747
2021-10-20	1720	0.0005	0.939	0.958	0.923	0.906	0.953	0.953	0.899	0.955	0.938	0.903	0.904	0.689	0.680
2021-11-06	1741	0.0002	0.939	0.945	0.940	0.922	0.961	0.927	0.899	0.953	0.933	0.910	0.892	0.723	0.693
Mean	1641	0.0006	0.943	0.958	0.929	0.918	0.957	0.923	0.927	0.958	0.925	0.922	0.899	0.685	0.720
SD	71	0.0003	0.007	0.010	0.026	0.023	0.007	0.024	0.027	0.006	0.020	0.020	0.020	0.115	0.081

Appendix B

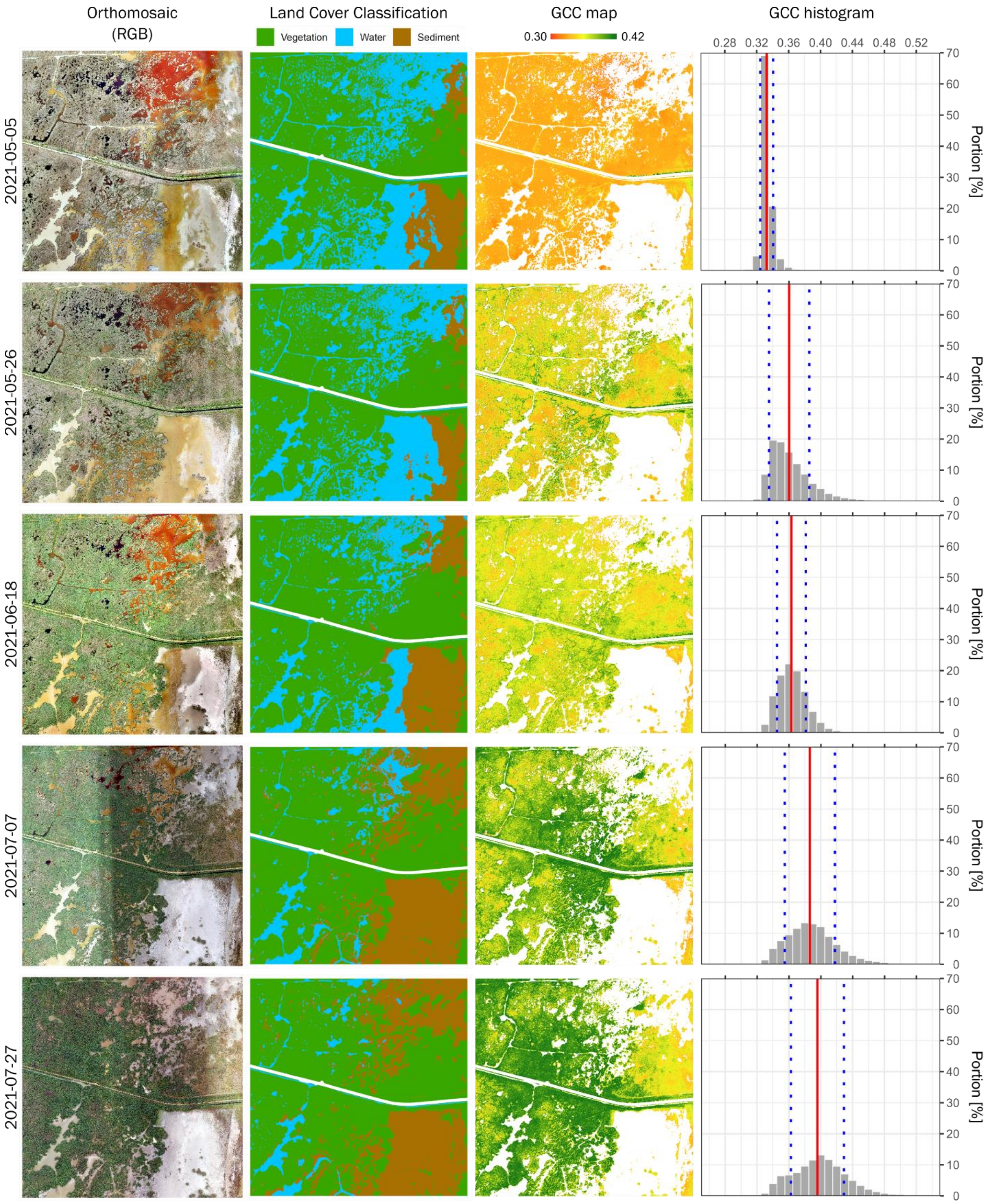

Figure A1. Spatio-temporal development of the study area in the reed ecosystem of Lake Neusiedl from May to July 2021. The mean GCC (red solid line) and the SD (blue dotted lines) of each flight date are shown in the GCC histogram.

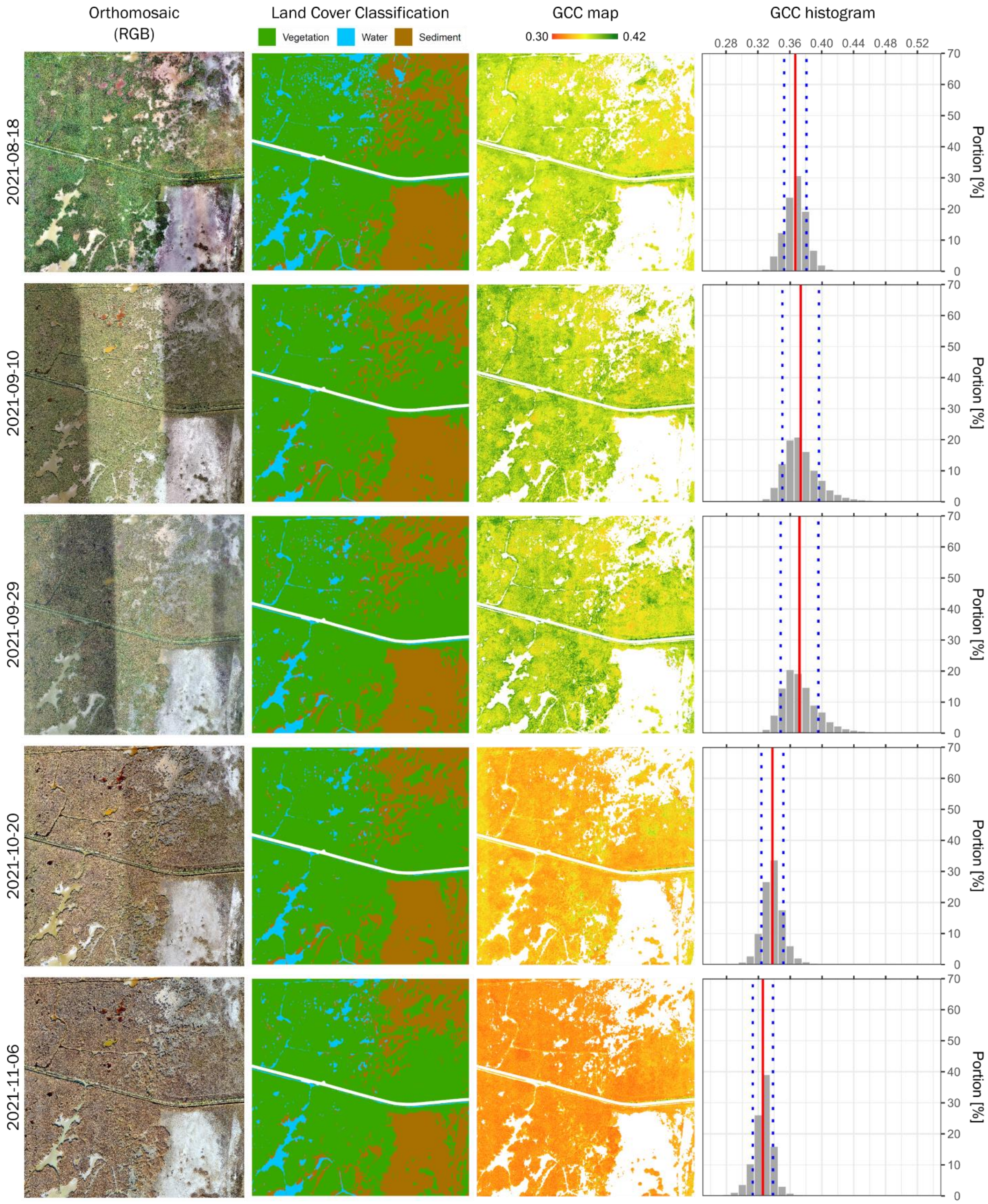

Figure A2. Spatio-temporal development of the study area in the reed ecosystem of Lake Neusiedl from August to November 2021. The mean GCC (red solid line) and the SD (blue dotted lines) of each flight date are shown in the GCC histogram.

Appendix C – Model training script

```
##################################################################################################
### Python script for training a deep learning model with arcgis.learn using jupyter notebook ###
##################################################################################################


# Import modules
import arcpy
from arcgis.learn import DeepLab, prepare_data


# Set the processor type environment to GPU
arcpy.env.processorType = "GPU"


# Prepare object from training sample exported by the Export Training Data tool in ArcGIS Pro
data = prepare_data(path = r'C:\path_to_training_sample_folder',
                    chip_size = 256,
                    val_split_pct = 0.2,
                    batch_size = 4,
                    stratify = True)


# Visualize training data
data.show_batch(alpha = 0.8)


# Setup the DeepLabV3+ model
model = DeepLab(data = data, pointrend = True)


# Run the learning rate finder to find optimum for training the model
model.lr_find()


# Train model for the specified number of epochs using specified learning rate
model.fit(epochs = 25,
          lr = 0.0004,
          early_stopping = False,
          checkpoint = False)


# Visualize ground truth and corresponding model prediction
model.show_results(alpha = 0.8)


# Calculate model accuracy
model.accuracy()


# Calculate mean IOU on the validation set for each class
model.mIOU()


# Save the model weights, create an Esri Model Definition and Deep Learning Package zip
model.save(
    name_or_path = r'C:\path_to_folder_where_model_should_be_saved',
    publish = True,
    compute_metrics = True,
    save_optimizer = True)
```

7 References

Aber, J.S.; Marzolff, I.; Ries, J.B. Small-Format Aerial Photography: Principles, Techniques and Geoscience Applications; Elsevier: Amsterdam [u.a.], **2010**; ISBN 978-0-444-53260-2.

Aggarwal, C.C. Neural Networks and Deep Learning : A Textbook; Springer: Cham, **2018**; ISBN 978-3-319-94462-3.

Al-Najjar, H.A.H.; Kalantar, B.; Pradhan, B.; Saeidi, V.; Halin, A.A.; Ueda, N.; Mansor, S. Land Cover Classification from Fused DSM and UAV Images Using Convolutional Neural Networks. *Remote Sensing* **2019**, *11*, 1461, doi:10.3390/rs11121461.

Albertz, J. Einführung in die Fernerkundung : Grundlagen der Interpretation von Luft- und Satellitenbildern; 3., aktualisierte und erw. Aufl.; Wiss. Buchges.: Darmstadt, **2007**; ISBN 978-3-534-19878-8.

Anagnostis, A.; Tagarakis, A.C.; Kateris, D.; Moysiadis, V.; Sørensen, C.G.; Pearson, S.; Bochtis, D. Orchard Mapping with Deep Learning Semantic Segmentation. *Sensors* **2021**, *21*, 3813, doi:10.3390/s21113813.

Badillo, S.; Banfai, B.; Birzele, F.; Davydov, I.I.; Hutchinson, L.; Kam-Thong, T.; Siebourg-Polster, J.; Steiert, B.; Zhang, J.D. An Introduction to Machine Learning. Clinical Pharmacology & Therapeutics **2020**, 107, 871–885, doi:10.1002/cpt.1796.

Baduge, S.; Thilakarathna, S.; Perera, J.; Arashpour, A.Prof.M.; Sharafi, P.; Teodosio, B.; Shringi, A.; Mendis, P. Artificial Intelligence and Smart Vision for Building and Construction 4.0: Machine and Deep Learning Methods and Applications. Automation in Construction **2022**, 141, 104440, doi:10.1016/j.autcon.2022.104440.

BEV. Bundesamt für Eich- und Vermessungswesen. 2019. Available online: https://www.bev.gv.at/ (accessed on 06 February 2024).

Beyer, F.; Jansen, F.; Jurasinski, G.; Koch, M.; Schröder, B.; Koebsch, F. Drought years in peatland rewetting: Rapid vegetation succession can maintain the net CO2 sink function. Biogeosciences 2021, 18, 917–935, doi:10.1080/01431161.2019.1580825.

Beyer, F.; Jurasinski, G.; Couwenberg, J.; Grenzdörffer, G. Multisensor Data to Derive Peatland Vegetation Communities Using a Fixed-Wing Unmanned Aerial Vehicle. *International Journal of Remote Sensing* **2019**, *40*, 9103–9125, doi:10.1080/01431161.2019.1580825.

Bhatnagar, S.; Gill, L.; Ghosh, B. Drone Image Segmentation Using Machine and Deep Learning for Mapping Raised Bog Vegetation Communities. *Remote Sensing* **2020**, *12*, 2602, doi:10.3390/rs12162602.

Blaschke, T. Object Based Image Analysis for Remote Sensing. *ISPRS Journal of Photogrammetry and Remote Sensing* **2010**, *65*, 2–16, doi:10.1016/j.isprsjprs.2009.06.004.

Campbell, J.B. Introduction to Remote Sensing; Sixth edition.; The Guilford Press: New York London, **2023**; ISBN 978-1-4625-4940-5.

Carrivick, J.L.; Smith, M.W.; Quincey, D.J. Structure from Motion in the Geosciences; New analytical methods in earth and environmental science; Wiley-Blackwell, **2016**; ISBN 1-118-89584-3.

Chang, J.; Clay, D. Matching Remote Sensing to Problems. In; **2016**; p. 22.

Chen, L.-C.; Zhu, Y.; Papandreou, G.; Schroff, F.; Adam, H. Encoder-Decoder with Atrous Separable Convolution for Semantic Image Segmentation, Available online: https://arxiv.org/abs/1802.02611v3 (accessed on 06 February 2024).

Chuvieco, E. Fundamentals of Satellite Remote Sensing : An Environmental Approach; Third edition.; CRC Press, Taylor and Francis Group: Boca Raton London New York, 2020; ISBN 978-0-429-01446-8.

Čížková, H.; Kučera, T.; Poulin, B.; Květ, J. Ecological Basis of Ecosystem Services and Management of Wetlands Dominated by Common Reed (Phragmites australis): European Perspective. Diversity **2023**, *15*, 629.

Csaplovics, E. Interpretation von Farbinfrarotbildern: Kartierung von Vegetationsschäden in Brixlegg; Schilfkartierung Neusiedler See. Geowiss. Mitteilungen **1982**, *23*, 178.

Csaplovics, E.; Nemeth, E. Airborne Optical Imaging in Support of Habitat Ecological Monitoring of the Austrian Reed Belt of Lake Neusiedl. In Proceedings of the GISScience RSGIS4HQ, Vienna, Austria, 23–25 September **2014**; pp. 163–167.

Csaplovics, E.; Schmidt, J. Schilfkartierung Neusiedler See: Ausdehnung und Struktur der Schilfbestände des Neusiedler Sees-Projektmanagement, Erfassung und Kartierung des österreichischen Anteiles durch Luftbildklassifikation, **2011**.

Davranche, A.; Poulin, B.; Lefebvre, G. Reedbed monitoring using classification trees and SPOT-5 seasonal time series. In Proceedings of the International Symposium on Advanced Methods of Monitoring Reed Habitats in Europe, Illmitz, Austria, 25–26 November **2010**; pp. 15–29.

Deliry, S.I.; Avdan, U. Accuracy of Unmanned Aerial Systems Photogrammetry and Structure from Motion in Surveying and Mapping: A Review. *J Indian Soc Remote Sens* **2021**, *49*, 1997–2017, doi:10.1007/s12524-021-01366-x.

Díaz-Delgado, R.; Cazacu, C.; Adamescu, M. Rapid Assessment of Ecological Integrity for LTER Wetland Sites by Using UAV Multispectral Mapping. *Drones* **2019**, *3*, 3, doi:10.3390/drones3010003.

Dienst, M.; Schmieder, K.; Ostendorp, W. Dynamik der Schilfröhrichte am Bodensee unter dem Einfluss von Wasserstandsvariationen. *Limnologica* **2004**, *34*, 29–36, doi:10.1016/S0075-9511(04)80019-7.

Dinka, M.; Ágoston-Szabó, E.; Szeglet, P. Comparison between biomass and C, N, P, S contents of vigorous and die-back reed stands of Lake Fertő/Neusiedler See. Biologia **2010**, 65, 237–247.

DJI. Mavic 2 Technische Daten. Available online: https://www.dji.com/at/mavic-2/info (accessed on 06 February 2024).

Dowle, M.; Srinivasan, A. Data.table: Extension of 'Data.Frame'; R Package Version 1.14.8; R Core Team: Vienna, Austria, 2023. Available online: https://CRAN.R-project.org/package=data.table (accessed on 06 February 2024).

ESRI Inc. ArcGIS Pro, Version 3.0.3; ESRI Inc.: Redlands, CA, USA, 2022.

ESRI. ArcGIS API for Python—Arcgis.learn Module. 2022. Available online: https://developers.arcgis.com/python/api-reference/arcgis.learn.toc.html#deeplab (accessed on 06 February 2024).

ESRI. Deep Learning Libraries for ArcGIS Pro 3.0.3. 2022. Available online: https://github.com/Esri/deep-learning-frameworks.git (accessed on 06 February 2024).

Filippa, G.; Cremonese, E.; Migliavacca, M.; Galvagno, M.; Folker, M.; Richardson, A.D.; Tomelleri, E. Package 'Phenopix': Process Digital Images of a Vegetation Cover; R Package Version 2.4.2; R Core Team: Vienna, Austria, 2020. Available online: https://cran.rstudio.com/web/packages/phenopix/phenopix.pdf (accessed on 06 February 2024).

Filippa, G.; Cremonese, E.; Migliavacca, M.; Galvagno, M.; Forkel, M.; Wingate, L.; Tomelleri, E.; Di Morra Cella, U.; Richardson, A.D. Phenopix: A R package for image-based vegetation phenology. Agric. For. Meteorol. 2016, 220, 141–150.

Fukarek, F.; Henker, H.; Berg, C. Flora von Mecklenburg-Vorpommern: Farn-und Blütenpflanzen; Weissdorn-Verlag: Jena, Germany, 2006.

Gili, P.; Civera, M.; Roy, R.; Surace, C. An Unmanned Lighter-Than-Air Platform for Large Scale Land Monitoring. Remote Sensing **2021**, 13, 2523, doi:10.3390/rs13132523.

Hackl, P.; Ledolter, J. A Statistical Analysis of the Water Levels at Lake Neusiedl. *AJS* **2023**, *52*, 87–100.

Hammer, U.T. Saline Lake Ecosystems of the World; Junk: Dordrecht, The Netherlands, 1986; p. 616.

Higgisson, W.; Cobb, A.; Tschierschke, A.; Dyer, F. Estimating the cover of Phragmites australis using unmanned aerial vehicles and neural networks in a semi–arid wetland. River Res. Appl. **2021**, *37*, 1312–1322.

Kallasvuo, M.; Lappalainen, A.; Urho, L. Coastal reed belts as fish reproduction habitats. Boreal Environ. Res. **2011**, *16*, 1–14.

Lillesand, T.M. Remote Sensing and Image Interpretation; 4. ed.; Wiley: New York, NY [u.a.], **2000**; ISBN 0-471-25515-7.

Lissner, J.; Schierup, H.-H. Effects of Salinity on the Growth of Phragmites Australis. A*quatic Botany* **1997**, *55*, 247–260, doi:10.1016/S0304-3770(96)01085-6.

Márkus, I.; Király, G. A Fertő magyarországi nádasainak minősítése, osztályozása és térképezése (Qualification, classification and mapping of the reed stands of the Hungarian part of Lake Fert˝o). In Monografikus Tanulmányok a Fertő és a Hanság vidékéről. (Monographic Studies of Lake Fertő and Hanság Area); Fertô–Hanság Nemzeti Park

Igazgatóság, Szaktudás Kiadó Ház: Budapest, Hungary, **2012**; pp. 73–81.

Klimkowska, A.; Van Diggelen, R.; Grootjans, A.P.; Kotowski, W. Prospects for fen meadow restoration on severely degraded fens. Perspect. Plant Ecol. Evol. Syst. **2010**, *12*, 245–255.

Koch, M.; Koebsch, F.; Hahn, J.; Jurasinski, G. From meadow to shallow lake: Monitoring secondary succession in a coastal fen after rewetting by flooding based on aerial imagery and plot data. Mires Peat **2017**, *19*, 1.

Manfreda, S.; McCabe, M.F.; Miller, P.E.; Lucas, R.; Pajuelo Madrigal, V.; Mallinis, G.; Ben Dor, E.; Helman, D.; Estes, L.; Ciraolo, G.; et al. On the Use of Unmanned Aerial Systems for Environmental Monitoring. Remote Sensing **2018**, 10, 641, doi:10.3390/rs10040641.

Meneses, N.C.; Baier, S.; Reidelstürz, P.; Geist, J.; Schneider, T. Modelling heights of sparse aquatic reed (Phragmites australis) using Structure from Motion point clouds derived from Rotary- and Fixed-Wing Unmanned Aerial Vehicle (UAV) data. Limnologica **2018**, *72*, 10–21.

Meneses, N.C.; Brunner, F.; Baier, S.; Geist, J.; Schneider, T. Quantification of Extent, Density, and Status of Aquatic Reed Beds Using Point Clouds Derived from UAV–RGB Imagery. Remote Sens. **2018**, *10*, 1869.

Mirtl, M.; Bahn, M.; Battin, T.; Borsdorf, A.; Dirnböck, T.; Englisch, M.; Erschbamer, B.; Fuchsberger, J.; Gaube, V.; Grabherr, G.; et al. Research for the Future LTER-Austria White Paper—On the Status and Orientation of Process Oriented Ecosystem Research, Biodiversity and Conservation Research and Socio-Ecological Research in Austria; Technical Report; LTER-Austria Series; LTER: Vienna, Austria, **2015**; Volume 2, ISBN 978-3-9503986-1-8. Available online: https://www.lter-austria.at (accessed on 06 February 2024).

Mitsch, W.J.; Bernal, B.; Hernandez, M.E. Ecosystem Services of Wetlands. *International Journal of Biodiversity Science, Ecosystem Services & Management* **2015**, *11*, 1–4, doi:10.1080/21513732.2015.1006250.

Nechwatal, J.; Wielgoss, A.; Mendgen, K. Flooding Events and Rising Water Temperatures Increase the Significance of the Reed Pathogen Pythium Phragmitis as a Contributing Factor in the Decline of Phragmites Australis. *Hydrobiologia* **2008**, *613*, 109–115, doi:10.1007/s10750-008-9476-z.

Nemeth, E.; Dvorak, M. Reed die-back and conservation of small reed birds at Lake Neusiedl, Austria. J. Ornithol. **2022**, *163*, 683–693.

Nemeth, E.; Dvorak, M.; Knoll, T.; Kohler, B.; Mühlbacher, S.; Werba, F. Managementplan für den Neusiedler See als Teil des Europaschutzgebiets Neusiedler See - Nordöstliches Leithagebirge. 2014.

Ostendorp, W. 'Die-Back' of Reeds in Europe — a Critical Review of Literature. *Aquatic Botany* **1989**, *35*, 5–26, doi:10.1016/0304-3770(89)90063-6.

Pashaei, M.; Kamangir, H.; Starek, M.J.; Tissot, P. Review and Evaluation of Deep Learning Architectures for Efficient Land Cover Mapping with UAS Hyper-Spatial Imagery: A Case Study Over a Wetland. *Remote Sensing* **2020**, *12*, 959, doi:10.3390/rs12060959.

Pettorelli, N.; Schulte to Buehne, H.; Shapiro, A.; Glover-Kapfer, P. Conservation Technology Series Issue 4: SATELLITE REMOTE SENSING FOR CONSERVATION; **2018**.

Pix4D Documentation. **2023**. Available online: https://support.pix4d.com/hc/en-us/sections/360003718571-How-to-step-bystep-instructions (accessed on 06 February 2024).

Pix4D SA (Ed.) What does step 1. Initial Processing do? **2022a**, URL: https://support.pix4d.com/hc/en-us/articles/202559339-What-does-step-1-Initial-Processing-do (accessed on 06 February 2024).

Pix4D SA (Ed.) Photo stitching vs orthomosaic generation. **2022b**, URL: https://support.pix4d.com/hc/en-us/articles/202558869-Photo-stitching-vs-orthomosaic-generation (accessed on 06 February 2024).

R Core Team. R: A Language and Environment for Statistical Computing: R Foundation for Statistical Computing; Version 4.2.2; R Core Team: Vienna, Austria, **2022**. Available online: https://www.R-project.org/ (accessed on 06 February 2024).

Rahman, M.A.; Wang, Y. Optimizing Intersection-Over-Union in Deep Neural Networks for Image Segmentation. In *Advances in Visual Computing*; Bebis, G., Boyle, R., Parvin, B., Koracin, D., Porikli, F., Skaff, S., Entezari, A., Min, J., Iwai, D., Sadagic, A., Scheidegger, C., Isenberg, T., Eds.; Lecture Notes in Computer Science; Springer International Publishing: Cham, **2016**; *10072*, 234–244, ISBN 978-3-319-50834-4.

Shen, F.; Zeng, G. Semantic Image Segmentation via Guidance of Image Classification. *Neurocomputing* **2019**, *330*, 259–266, doi:10.1016/j.neucom.2018.11.027.

Soja, G.; Züger, J.; Knoflacher, M.; Kinner, P.; Soja, A.-M. Climate Impacts on Water Balance of a Shallow Steppe Lake in Eastern Austria (Lake Neusiedl). *Journal of Hydrology* **2013**, *480*, 115–124, doi:10.1016/j.jhydrol.2012.12.013.

Sonnentag, O.; Hufkens, K.; Teshera-Sterne, C.; Young, A.M.; Friedl, M.; Braswell, B.H.; Milliman, T.; O'Keefe, J.; Richardson, A.D. Digital Repeat Photography for Phenological Research in Forest Ecosystems. *Agricultural and Forest Meteorology* **2012**, *152*, 159–177, doi:10.1016/j.agrformet.2011.09.009.

Steiner, G.M.; Englmaier, P.; Fink, M.; Grünweis, F.; Höfner, I.; Korner, I.; Ströhle, A.; Wolf, W. Mittelpunkte der Moorflächen aus dem Moorschutzkatalog. **1992**. Bundesministerium für Gesundheit und Umweltschutz, Wien. Available online: https://www.data.gv.at/katalog/de/dataset/moorschutzkatalog_1992_points (accessed on 06 February 2024)

Sun, C.; Li, J.; Liu, Y.; Zhao, S.; Zheng, J.; Zhang, S. Tracking annual changes in the distribution and composition of saltmarsh vegetation on the Jiangsu coast of China using Landsat time series–based phenological parameters. Remote Sens. Environ. **2023**, *284*, 113370.

Szeliski, R. Computer Vision: Algorithms and Applications; Texts in Computer Science; 1st ed.; Springer Nature: London, **2010**; ISBN 978-1-84882-935-0.

Tabian, I.; Fu, H.; Sharif Khodaei, Z. A Convolutional Neural Network for Impact Detection and Characterization of Complex Composite Structures. Sensors **2019**, 19, 4933, doi:10.3390/s19224933.

Tiškus, E.; Vaičiūtė, D.; Bučas, M.; Gintauskas, J. Evaluation of common reed (Phragmites australis) bed changes in the context of management using earth observation and automatic threshold. Eur. J. Remote Sens. **2023**, *56*, 2161070,

Tong, X.-Y.; Xia, G.-S.; Lu, Q.; Shen, H.; Li, S.; You, S.; Zhang, L. Land-Cover Classification with High-Resolution Remote Sensing Images Using Transferable Deep Models. *Remote Sensing of Environment* **2020**, *237*, 111322, doi:10.1016/j.rse.2019.111322.

Trimble R1—Datasheet, Model 2 GNSS SYSTEMS. Available online: https://geospatial.trimble.com/sites/geospatial.trimble.com/files/2021-07/022516-332B_TrimbleR10-2_DS_USL_0721_LR.pdf (accessed on 25 May 2023).

van Diggelen, R.; Middleton, B.; Bakker, J.; Grootjans, A.; Wassen, M. Fens and floodplains of the temperate zone: Present status, threats, conservation and restoration. Appl. Veg. Sci. **2006**, *9*, 157–162.

van Iersel, W.; Straatsma, M.; Addink, E.; Middelkoop, H. Monitoring height and greenness of non-woody floodplain vegetation with UAV time series. ISPRS J. Photogramm. Remote Sens. **2018**, *141*, 112–123.

Villa, P.; Laini, A.; Bresciani, M.; Bolpagni, R. A remote sensing approach to monitor the conservation status of lacustrine Phragmites australis beds. Wetl. Ecol. Manag. **2013**, *21*, 399–416.

Villanueva, J.K.S.; Blanco, A.C. Optimization of ground control point (GCP) configuration for unmanned aerial vehicle (UAV) survey using structure from motion (SfM). Int. Arch. Photogramm. Remote. Sens. Spat. Inf. Sci. **2019**, *XLII-4/W12*, 167–174, doi:10.5194/isprs-archives-XLII-4-W12-167-2019.

Volpi, M.; Tuia, D. Dense Semantic Labeling of Subdecimeter Resolution Images With Convolutional Neural Networks. *IEEE Trans. Geosci. Remote Sensing* **2017**, *55*, 881–893, doi:10.1109/TGRS.2016.2616585.

Wasserportal Burgenland. Niederschlag: Illmitz-Biologische Station. **2023**. Available online: https://wasser.bgld.gv.at/hydrographie/der-niederschlag/illmitz-biologische-station(accessed on 06 February 2024).

Westoby, M.J.; Brasington, J.; Glasser, N.F.; Hambrey, M.J.; Reynolds, J.M. 'Structure-from-Motion' Photogrammetry: A Low-Cost, Effective Tool for Geoscience Applications. *Geomorphology* **2012**, *179*, 300–314, doi:10.1016/j.geomorph.2012.08.021.

Wickham, H. ggplot2: Elegant Graphics for Data Analysis; Springer: New York, NY, USA, **2016**. Available online: https://ggplot2.tidyverse.org (accessed on 06 February 2024).

Wolfram, G.; Herzig, A. Nährstoffbilanz Neusiedler See. Wien. Mitteilungen **2013**, *228*, 317–338.

Yu, G.A.; Li, Z.; Yang, H.; Lu, J.; Huang, H.Q.; Yi, Y. Effects of riparian plant roots on the unconsolidated bank stability of meandering channels in the Tarim River, China. Geomorphology **2020**, *351*, 106958.

Zhang, X.; Han, L.; Han, L.; Zhu, L. How Well Do Deep Learning-Based Methods for Land Cover Classification and Object Detection Perform on High Resolution Remote Sensing Imagery? *Remote Sensing* **2020**, *12*, 417, doi:10.3390/rs12030417.

Zhao, W.; Du, S. Learning Multiscale and Deep Representations for Classifying Remotely Sensed Imagery. *ISPRS Journal of Photogrammetry and Remote Sensing* **2016**, *113*, 155–165, doi:10.1016/j.isprsjprs.2016.01.004.

Zheng, J.-Y.; Hao, Y.-Y.; Wang, Y.-C.; Zhou, S.-Q.; Wu, W.-B.; Yuan, Q.; Gao, Y.; Guo, H.-Q.; Cai, X.-X.; Zhao, B. Coastal Wetland Vegetation Classification Using Pixel-Based, Object-Based and Deep Learning Methods Based on RGB-UAV. *Land* **2022**, *11*, 2039, doi:10.3390/land11112039.

Zlinszky, A. Mapping and conservation of the reed wetlands on Lake Balaton. Ph.D. Thesis, Eötvös Loránd University, Budapest, Hungary, **2013**.